Astronomy Department Faculty Publication Series   Astronomy

2009

Powerful H$_2$ Line-cooling in Stephan's Quintet : I - Mapping the Significant Cooling Pathways in Group-wide Shocks

ME Cluver

PN Appleton

F Boulanger

P Guillard

P Ogle

See next page for additional authors

Authors

ME Cluver, PN Appleton, F Boulanger, P Guillard, P Ogle, P-A Duc, N Lu, J Rasmussen, WT Reach, JD Smith, R Tuffs, CK Xu, and Min Yun

POWERFUL H₂ LINE-COOLING IN STEPHAN'S QUINTET : I - MAPPING THE SIGNIFICANT COOLING PATHWAYS IN GROUP-WIDE SHOCKS

M.E. Cluver[1], P.N. Appleton[2,3], F. Boulanger[4], P. Guillard[4], P. Ogle[1], P.-A., Duc[5], N. Lu[2], J. Rasmussen[6], W.T. Reach[1], J.D. Smith[7], R. Tuffs[8], C.K. Xu[2], M.S. Yun[9]

ABSTRACT

We present results from the mid-infrared spectral mapping of Stephan's Quintet using the *Spitzer Space Telescope*[10]. A $1000\,\mathrm{km\,s^{-1}}$ collision ($t_{col} = 5 \times 10^6$ yr) has produced a group-wide shock and for the first time the large-scale distribution of warm molecular hydrogen emission is revealed, as well as its close association with known shock structures. In the main shock region alone we find $5.0 \times 10^8\,M_\odot$ of warm H₂ spread over $\sim 480\,\mathrm{kpc^2}$ and additionally report the discovery of a second major shock-excited H₂ feature, likely a remnant of previous tidal interactions. This brings the total H₂ line luminosity of the group in excess of $10^{42}\,\mathrm{erg\,s^{-1}}$. In the main shock, the H₂ line luminosity exceeds, by a factor of three, the X-ray luminosity from the hot shocked gas, confirming that the H₂-cooling pathway dominates over the X-ray. [Si II]$34.82\mu m$ emission, detected at a luminosity of 1/10th of that of the H₂, appears to trace the group-wide shock closely and in addition, we detect weak [Fe II]$25.99\mu m$ emission from the most X-ray luminous part of the shock. Comparison with shock models reveals that this emission is consistent with regions of fast shocks ($100 < V_s < 300\,\mathrm{km\,s^{-1}}$) experiencing depletion of iron and silicon onto dust grains.

Star formation in the shock (as traced via ionic lines, PAH and dust emission) appears in the intruder galaxy, but most strikingly at either end of the radio shock. The shock ridge itself shows little star formation, consistent with a model in which the tremendous H₂ power is driven by turbulent energy transfer from motions in a post-shocked layer which suppresses star formation. The significance of the molecular hydrogen lines over other measured sources of cooling in fast galaxy-scale shocks may have crucial implications for the cooling of gas in the assembly of the first galaxies.

Subject headings: galaxies: evolution – galaxies: individual (NGC 7318b; NGC7319) – galaxies: interactions – galaxies: intergalactic medium – physical data and processes: shock waves

1. INTRODUCTION

Stephan's Quintet (hereafter SQ) is a strongly interacting compact group which has produced a highly disturbed intragroup medium (IGM) (Xu et al. 2003, 2005) through a complex sequence of interactions and harrassment (Allen & Sullivan 1980; Williams et al. 2002). This interplay has produced a large-scale intergalactic shock-wave, first observed as a narrow filament in the

[1] Spitzer Science Center, IPAC, California Institute of Technology, Pasadena, CA 91125
[2] NASA Herschel Science Center, IPAC, California Institute of Technology, Pasadena, CA 91125
[3] Visiting Astronomer, Institute d'Astrophysique Spatiale, Université Paris Sud 11, Orsay, France
[4] Institute d'Astrophysique Spatiale, Universite Paris Sud 11, Orsay, France
[5] Laboratoire AIM, CEA/DSM - CNRS - Université Paris Diderot, DAPNIA/Service d'Astrophysique, CEA/Saclay, F-91191 Gif-sur-Yvette Cedex, France
[6] Carnegie Observatories, 813 Santa Barbara St., Pasadena, CA 91101, Chandra Fellow
[7] Department of Physics and Astronomy, Mail Drop 111, University of Toledo, 2801 West Bancroft Street, Toledo, OH 43606
[8] Max-Planck-Institut für Kernphysik, Saupfercheckweg 1, 69117 Heidelberg,Germany
[9] Department of Astronomy, University of Massachusetts, Amherst, MA
[10] This work is based on observations made with the *Spitzer* Space Telescope, which is operated by the Jet Propulsion Laboratory, California Institute of Technology under NASA contract 1407. Support for this work was provided by NASA through an award issued by JPL/Caltech.

radio continuum (Allen & Hartsuiker 1972), and subsequently detected in the X-ray (Pietsch et al. 1997; Trinchieri et al. 2005; O'Sullivan et al. 2009). The high-velocity ($\sim$1000 km s^{-1}) collision of an intruder galaxy, NGC 7318b, with the intergalactic medium of the group (Sulentic et al. 2001; Xu et al. 2003) is believed to be responsible for the shock-heating of the X-ray emitting gas. Optical emission line ratios and observed broad linewidths provide evidence that the region is powered by strong shocks and not star formation (Xu et al. 2003; Duc et al. 2010, in preparation).

The main elements of Stephan's Quintet are shown in Figure 1. Central to the system is the primary shock, as defined by the 20 cm radio continuum emission. NGC 7318b, the intruder galaxy, lies to the West of the shock, while the large Seyfert 2 galaxy (Durret 1994), lies to the East. Other members of the group are also indicated. The peculiar extranuclear star formation region, named SQ-A (Xu et al. 1999, 2003), lies at the extreme northern end of the main shock wave. NGC 7318a (west of NGC 7318b) is also a strongly interacting group member, with NGC 7317 further away from the core.

The unexpected discovery of extremely powerful, pure-rotational H₂ line emission from the center of the shock (Appleton et al. 2006), using the *Spitzer Space Telescope* (Werner et al. 2004), has sparked intense interest in the SQ system. Warm molecular hydrogen emission was found with a line luminosity exceeding the X-ray lu-
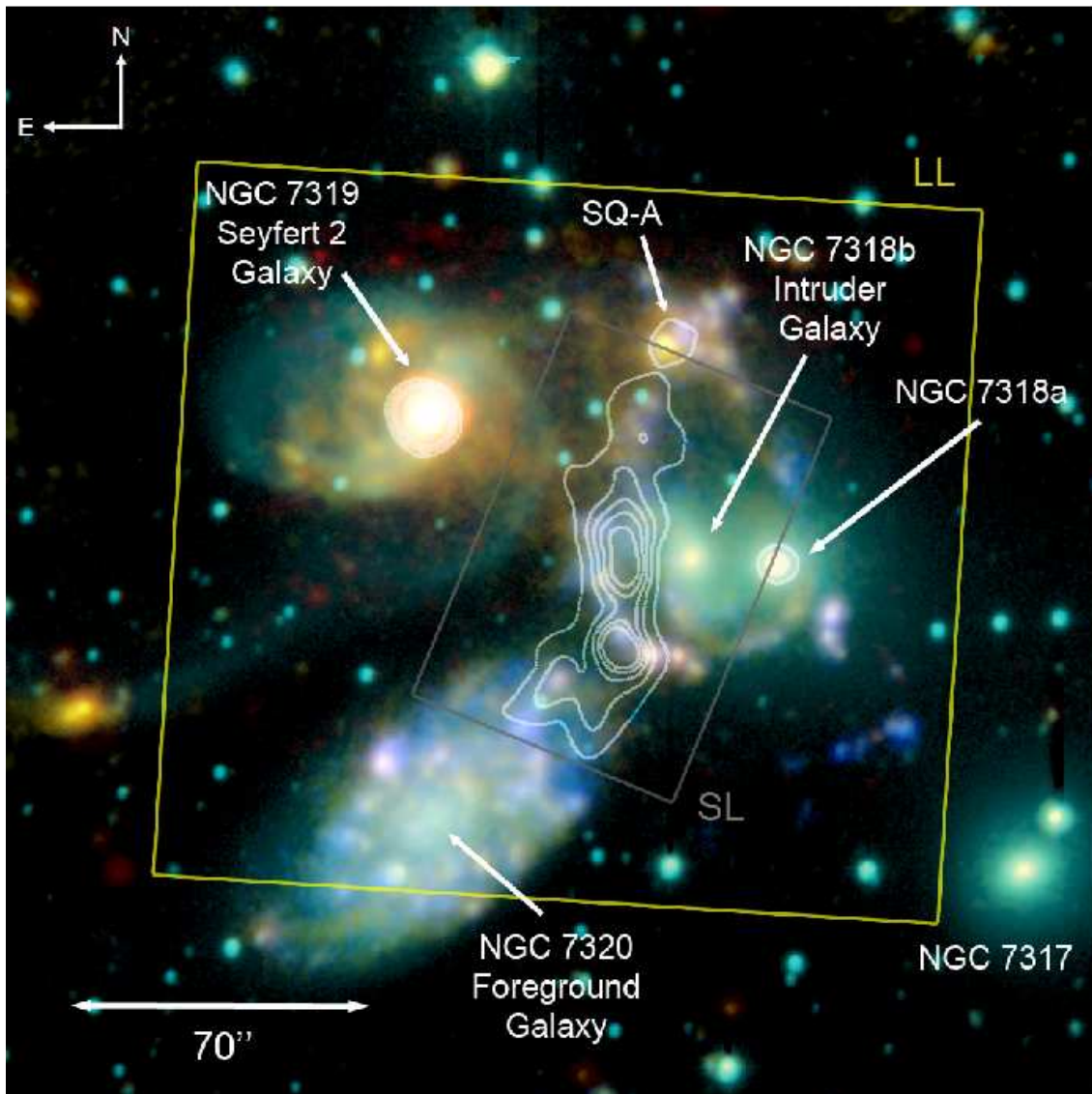
FIG. 1.— Schematic composite image of Stephan's Quintet consisting of a *Galex* Near-UV image (blue), an optical R-band image (cyan) from Xu et al. (1999), an IRAC 8μm image (yellow) and an image from the 16μm IRS Peak-up Array (red). The contours represent the 20 cm emission associated with the shock as obtained by the VLA (Xu et al. 2003). The boundaries of the *Spitzer* IRS Spectral Mapping coverage (this paper) are shown as boxes. A color version of this image is available in the online publication.

minosity from the shock. The mid-infrared (MIR) H$_2$ linewidth was resolved ($\sigma = 870$ km s^{-1}) suggesting that the H$_2$-emitting clouds carry a large bulk-kinetic energy, tapping a large percentage of the energy available in the shock. A recent model of SQ, involving the collision between two inhomogeneous gas flows, describes H$_2$ formation out of the multiphase, shocked gas, and an efficient cooling channel for high-speed shocks as an alternative to X-ray emission (Guillard et al. 2009)

Since the SQ detection, several other systems exhibiting similarly strong H$_2$ emission have been discovered. Ogle et al. (2007, 2009) find that a large-subset of the local 3CR radio galaxies have extremely dominant MIR rotational H$_2$ lines, often seen against a very weak thermal continuum. The low AGN and star formation power are insufficient to drive the MIR H$_2$ emission. Mechanical heating driven by the radio jet interaction with the

host galaxy ISM is the favoured mechanism. In addition, total H$_2$ luminosities in the range $10^{41} - 10^{43}$ ergs s^{-1} have been detected in some central cluster galaxies out to $z \sim 0.3$ (Egami et al. 2006, G. de Messieres - University of Virginia, Private communication) and in filaments in clusters (Hatch et al. 2005). The study of nearby prototypes may provide valuable insight into the nature of these more distant systems. The large scale (~ 30 kpc) of the SQ shock is well-suited for such a study.

In this Paper I, we extend the single pointing observations of Appleton et al. (2006) to full spectral maps of SQ using the IRS instrument on the *Spitzer* Space Telescope, hereafter *Spitzer*. In Paper II, we will present detailed 2-dimensional excitation maps of the H$_2$ emission across the face of the X-ray emitting shock, and compare them with models. In addition, several other papers are being prepared by our team which will discuss the relationship

between the UV/X-ray emission and emission from dust.

In Section 2, we present our observations and data reduction methods. In Section 3 we discuss the mapping results for various detected lines. In Sections 4, 5 and 6 we present our discussion on the properties of the system and in Section 7 the implication for galaxy formation. In Section 8 we present our conclusions. Additional material is included as appendices, with a discussion on NGC 7319 in Appendix A, and a reanalysis of the high resolution MIR spectrum of the shock, as well as renanalysis of the X-ray data presented in Appendix B and C, respectively.

Throughout this paper, we assume a systemic velocity of $v = 6600 \, \mathrm{km \, s^{-1}}$ for the group, corresponding to a distance of 94 Mpc with $H_{\mathrm{o}} = 70 \, \mathrm{km \, s^{-1} Mpc^{-1}}$.

2. OBSERVATIONS AND DATA REDUCTION

Mid-infrared spectroscopy of the shock region in SQ was obtained using the IRS instrument (Houck et al. 2004) onboard *Spitzer*. Observations were done in low-resolution mapping mode, using the Short-Low ($R \sim 60 - 127$; $5.2 - 14.5 \, \mu$m) and Long-Low ($R \sim 57 - 126$; $14.0 - 38.0 \, \mu$m) modules and taken on January 11 2008 and December 10 2007, respectively. Figure 1 displays the outline of the areas observed superimposed on a composite image of the group.

The SL spectral mapping consists of two separate, partially overlapping maps, centered North and South on the X-ray emission associated with the shock. The map was constructed with 23 steps of $2.8''(0.75 \times$ slit width) perpendicular to the slit and one parallel step of $7.2''$. Observations consisted of $60 \, \mathrm{s}$ integrations with 5 cycles per step.

The LL module was used to map an area of $\sim 2.8' \times 3.2'$ using 21 steps of $8.0''$ ($0.75 \times$ slit width) perpendicular to the slit and a parallel step of $24.0''$. An integration time of $120 \, \mathrm{s}$ was used with 3 cycles per step.

Primary data reductions were done by the *Spitzer* Science Center (SSC) pipeline, version S17.0.4 and S17.2.0 for SL and LL respectively, which performs standard reductions such as ramp fitting, dark current subtraction and flat-fielding. Background subtraction for LL data was performed by subtracting dedicated off-source observations, with the same observing mode, taken shortly after the mapping sequence. In the case of SL, where for scheduling reasons the dedicated "off" observations were too far away in time to be optimal, backgrounds were generated from observations at the periphery of the map that contain no spectral line signatures.

Examination of the pipeline products showed that the stray-light-corrected images (that account for potential spillover from the peak-up arrays onto the SL1/2 spectral apertures) contained wavelength-dependent over-corrections in some of the images, seemingly due to a high background of cosmic rays during the SL portion of the mapping. To negate this effect, the alternative flat-fielded images (also available from the science pipeline) that are uncorrected for crosstalk and straylight removal were used. It was determined that after background subtraction, any uncorrected stray light in the SL spectral extraction areas was unmeasurable at the $< 2 - 3\%$ level. Thus stray-light correction was unneccesary, and the resulting Basic Calibrated Data (BCD) images used were of better quality than the standard BCDs.

For all modules, individual frames for each pointing were median-combined and obvious "bad" pixels were replaced using customised software that allows for manual "average" replacement. The spectra were assembled into spectral cubes for each module using the software tool, CUBISM (Smith et al. 2007). Further bad pixel removal was performed within CUBISM. Spectral maps were generated by making continuum maps on either side of a feature and subtracting the averaged continuum map from the relevant emission line map. One dimensional spectra were further extracted from the data cubes using matched apertures.

Broad-band images at 16 and 24μm were obtained with the *Spitzer* IRS blue Peak-up Imager (PUI) and the MIPS instrument. The PUI was obtained in a 5 x 5 map with 3 cycles of $30 \, \mathrm{s}$ duration each on 2007 December 10. The MIPS instrument (Rieke et al. 2004) on *Spitzer* obtained 24μm imaging of SQ on 2008 July 29, achieving a spatial resolution of $\sim 6''$. Primary data reduction was done by the *Spitzer* Science Center (SSC) science pipeline (version S18.0.2) run through the MOPEX software, and for the MIPS image a smooth 2D polynomial background was further removed to correct for a large-scale background gradient. *Spitzer* IRAC 3.6, 4.5, 5.8 and 8.0 μm data of SQ (P.I. J.R. Houck) were obtained from the SSC archive; these were reduced using science pipeline version S18.0.2. The final mosaics have a pixel scale of $0.61''$.

3. RESULTS

3.1. *The Molecular Hydrogen Distribution*

The pure rotational transitions of molecular hydrogen can be excited by several mechanisms. These include FUV (Far Ultraviolet) induced pumping, and possible additional collisional heating, of the H$_2$ in photodissociation regions associated with star formation (e. g. Black & van Dishoeck 1987, Hollenbach & Tielens 1997), hard X-rays penetrating and heating regions within molecular clouds, which in turn excite H$_2$ via collisions with electrons or hydrogen atoms (Lepp & McCray 1983; Draine & Woods 1992) and finally collisional excitation of H$_2$ due to acceleration produced by shocks (e.g. Shull & Hollenbach 1978). The pure rotational MIR line ratios are not especially good diagnostics for distinguishing between these mechanisms since all three mechanisms discussed can lead to well thermalized level distributions of lower-level rotational states. The rotational H$_2$ emission lines do, however, allow us to trace gas at different temperatures and compare with model predictions (this will be the main emphasis of Paper II). Higher level transitions 0-0 S(3)-S(5) tend to trace warmer gas, whereas the S(0) and S(1) lines are sensitive to the "coolest" warm H$_2$.

Although the line ratios themselves cannot be used directly as shock diagnostics, in Stephan's Quintet the distribution of large-scale X-ray and radio emission, plus optical emission line diagnostics, provide strong evidence that the giant filament seen in Figure 1 is the result of a strong shock. In Appleton et al. (2006) this fact was used to reveal the surprising association of detected H$_2$ emission with the shock. However, in this paper we can make a more definitive association of the emission with the shock by means of spectral maps.
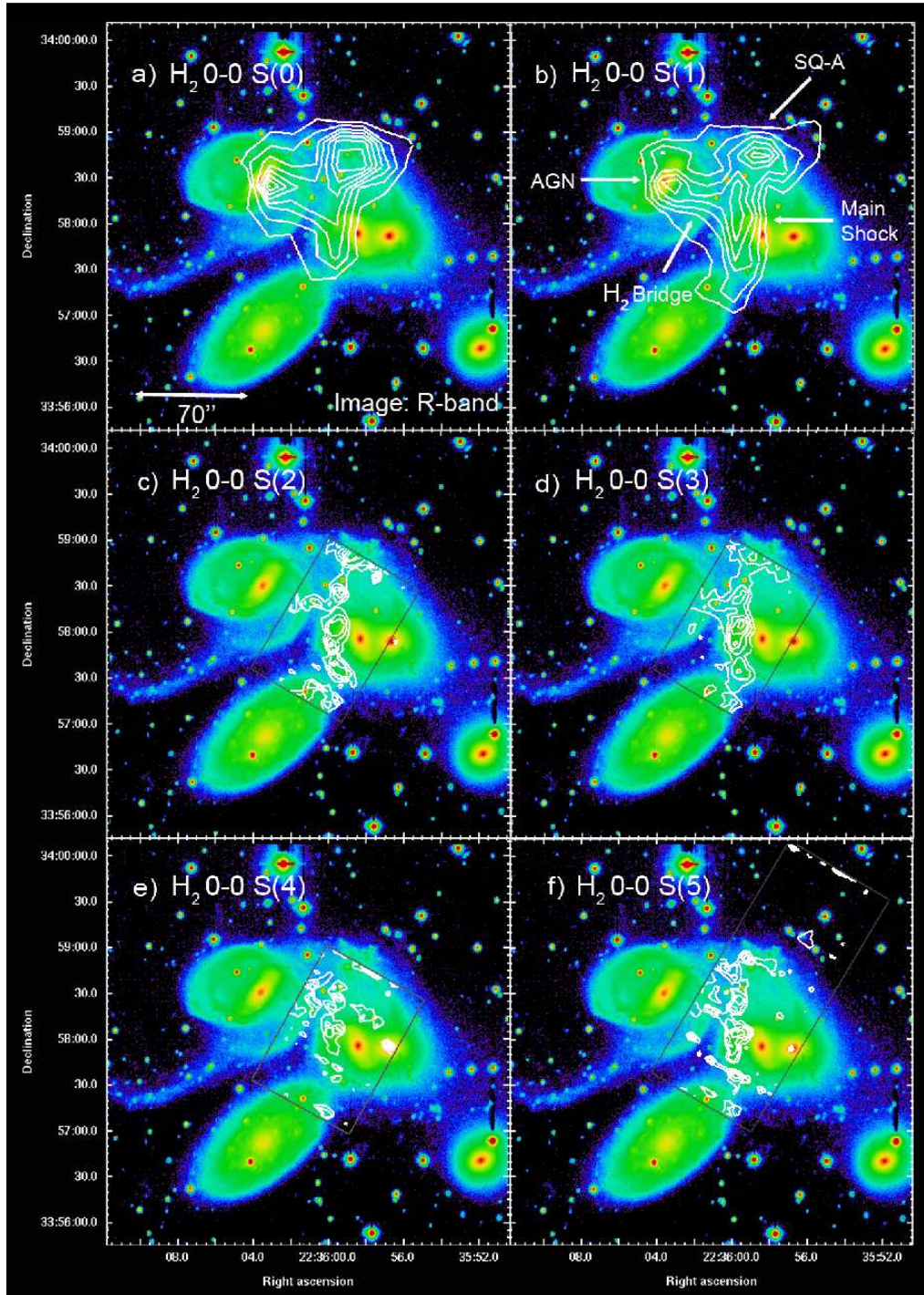
FIG. 2.— The large-scale distribution of warm H₂ in Stephan's Quintet with each detected 0-0 transition overlaid on an *R*-band image from Xu et al. (1999). The grey box indicates the limit of the SL module coverage. Contour levels are as follows (all in units of MJy/sr): (a) 0.1, 0.14. 0.19, 0.28, 0.32, 0.37, 0.41, 0.46, 0.5, (b) 0.3, 0.53, 0.75, 0.98, 1.2, 1.43, 1.65, 1.88, 2.1, (c) 0.3, 0.4, 0.5, 0.6, 0.7, (d) 0.25, 0.42, 0.58, 0.75, 0.92, 1.08, 1.25, (e) 0.11, 0.19, 0.27, 0.36, 0.44, 0.52, 0.6 and (f) 0.3, 0.46, 0.61, 0.77. 0.93, 1.09, 1.24, 1.4. The SL coverage for (f) is larger due to incorporating the "parallel mode" SL2 slit observations from the "off-target" positions when SL1 mapping observations were the primary observing mode.

The spectral cubes were used to extract maps of all the pure rotational emission lines of molecular hydrogen that were detected, namely the 0-0 S(0) 28.22μm, S(1) 17.03μm, S(2) 12.28μm, S(3) 9.66μm, S(4) 8.03μm and S(5) 6.91μm lines. Specific intensity contour maps of these lines are presented in Figure 2 overlaid on a R-band image of the region from Xu et al. (1999). The S(0) and S(1) lines were mapped by the LL modules, while S(2) - S(5) transitions were mapped by the SL modules of the IRS. As indicated in Figure 1, the SL observations were concentrated on the main shock to provide high signal to noise (S/N) measurements there. As a result, these maps do not fully cover SQ-A or NGC 7319. We note that the S(4) line at 8.03μm (Fig. 2e) is faint, and also suffers from contamination from the PAH bands at 7.7μm and 8.6μm.

The contours indicate powerful, widespread emission running North-South along the shock ridge (see Fig. 1). In addition we detect strong emission from the star forming region, SQ-A, as well as associated with NGC 7319. We discuss further details of the AGN-like MIR emission lines from NGC 7319 in Appendix A.

Figures 2a-d reveal a new H$_2$ structure running eastward from the "main" shock ridge. In what follows, we refer to this feature as the "bridge". This structure is observed faintly in the *Chandra* (Trinchieri et al. 2003) and XMM (Trinchieri et al. 2005) X-ray images and detected as faint Hα emission by Xu et al. (2003), but is not strong in radio continuum images.

As is evident in Figure 2, there is distinct variation in the distribution of the warm H$_2$ emission. The brightest 0-0 S(0) emission (Fig. 2a) appears to be concentrated towards the North of the shock, whereas the 0-0 S(1) transition emission (Fig. 2b) appears more concentrated towards the center. The S(0) and S(1) maps demonstrate that the H$_2$ in the bridge terminates in a large clump a few arcsecs west of the nucleus of the Seyfert 2 galaxy NGC 7319, and in a small detour to the North (especially in the S(1) map which has the highest S/N).

The S(2) through S(5) lines clearly show that the warm H$_2$ emission breaks into clumps in the shock. Despite the limited coverage compared to the LL mapping, the base of the "bridge" is visible and SQ-A is partially covered. SQ-A is fully covered by the SL2 module (because of fortuitous "off observation" coverage) and hence the S(5) emission line reveals that in SQ-A the H$_2$ emission is also clumpy.

The molecular-line maps provide considerable information about the excitation of the H$_2$ along and across the X-ray shock, but these discussions will be deferred to a full 2-D modelling of the H$_2$ excitation in Paper II (Appleton et al., in preparation). Instead we shall limit ourselves to global properties of the H$_2$ here. In Section 4 we shall present spectra of some selected regions of the emission and discuss a global excitation diagram for the shock.

To further demonstrate the close connection between the H$_2$ emission and the main global shock-wave in SQ, we now consider the distribution of warm H$_2$ in relation to the X-ray and radio emission. Figure 3a and b show the S(0) and S(3) contours overlaid on an XMM-Newton X-ray image (Trinchieri et al. 2005) of Stephan's Quintet. The warm molecular hydrogen is distributed along the length of the main North-South (NS) X-ray shock

ridge and along the "bridge", demonstrating the remarkable projected coexistence of of hot X-ray plasma ($10^6 <$ T $< 10^7$ K) and warm H$_2$ ($10^2 <$ T$< 10^3$ K). Although the H$_2$ appears to follow the X-ray, there are subtle differences. The cooler S(0) line has emission concentrated to the North and follows the X-ray less closely compared to the warmer S(3) line. The S(3) line exhibits a clear correspondence to the X-ray, notably at the center of the shock, where we find peaks at both wavelengths. Thus the region of greatest shock heating, as traced by the stronger X-ray emission, appears to correspond to the higher-J H$_2$ transitions, perhaps implying a causal connection. The intergalactic star formation region SQ-A, is essentially absent in X-ray emission, as seen in Figure 3a, but is strongly detected in H$_2$.

We find a similar picture in the radio continuum (Fig. 3c & d) with the S(0) line demonstrating correspondence with the main shock, but dominated by emission in the North where we observe less powerful radio emission. The S(3) (and S(2)–see Fig. 2c) line presents a much tighter correlation with regions of the shock that are more radio luminous than the lower-J transitions. The radio emission is quite likely sensitive to the most compressed regions of the shock where cosmic ray particles are accelerated more strongly (Helou & Bicay 1993; Appleton et al. 1999), whereas the brightest X-ray patches are likely due to the fastest regions of the shock (Guillard et al. 2009). As already mentioned the "bridge" emission is detected only faintly in the X-ray and is weak or absent at radio continuum wavelengths. This noticeable difference compared to the main shock likely implies that the conditions that give rise to strong synchrotron emission in the main shock are absent in the bridge.

3.2. *Shock-related Fine-structure Line Emission*

Emission from fine-structure lines provide key diagnostics that trace the interplay between the various constituents of the shocked interstellar medium. In Appleton et al. (2006) the spectra were limited to the very core of the shock and only weak emission was detected from all but two metal lines, namely [Ne II]12.81μm and [Si II]34.82μm (this data has been reanalysed and is presented in Appendix B). In this section we discuss the spatial distribution of emission from the [Fe II]25.99μm, [O IV]25.89μm, [S III]33.48μm, [Si II]34.82μm, [Ne II]12.81μm and [Ne III]15.56 μm lines.

In Figure 4 we present the specific intensity contours of the [Fe II]25.99μm and [O IV]25.89μm blend, [S III]33.48μm and [Si II]34.82μm emission lines.

Given the low spectral resolution of the SL and LL modules of *Spitzer*, we cannot distinguish between emission from [Fe II]25.99μm and [O IV]25.89μm. However, except in the direction of the Seyfert II galaxy NGC 7319, the emission near 26μm seen in Figure 4a is likely to be pure [Fe II] with little contamination from [O IV] as there is no evidence from the spectra of high-excitation emission from the intragroup medium in SQ. For example, [O IV] has an excitation potential of 56 eV (compared to 7.9 eV of [Fe II]), and yet Appleton et al. (2006) have shown that the [Ne III]/[Ne II] ratio is low suggesting low-excitation conditions for the ions in the shock, further supported in Section 5. Assuming that, apart from towards NGC 7319, [Fe II] dominates the [Fe II]+[O IV]
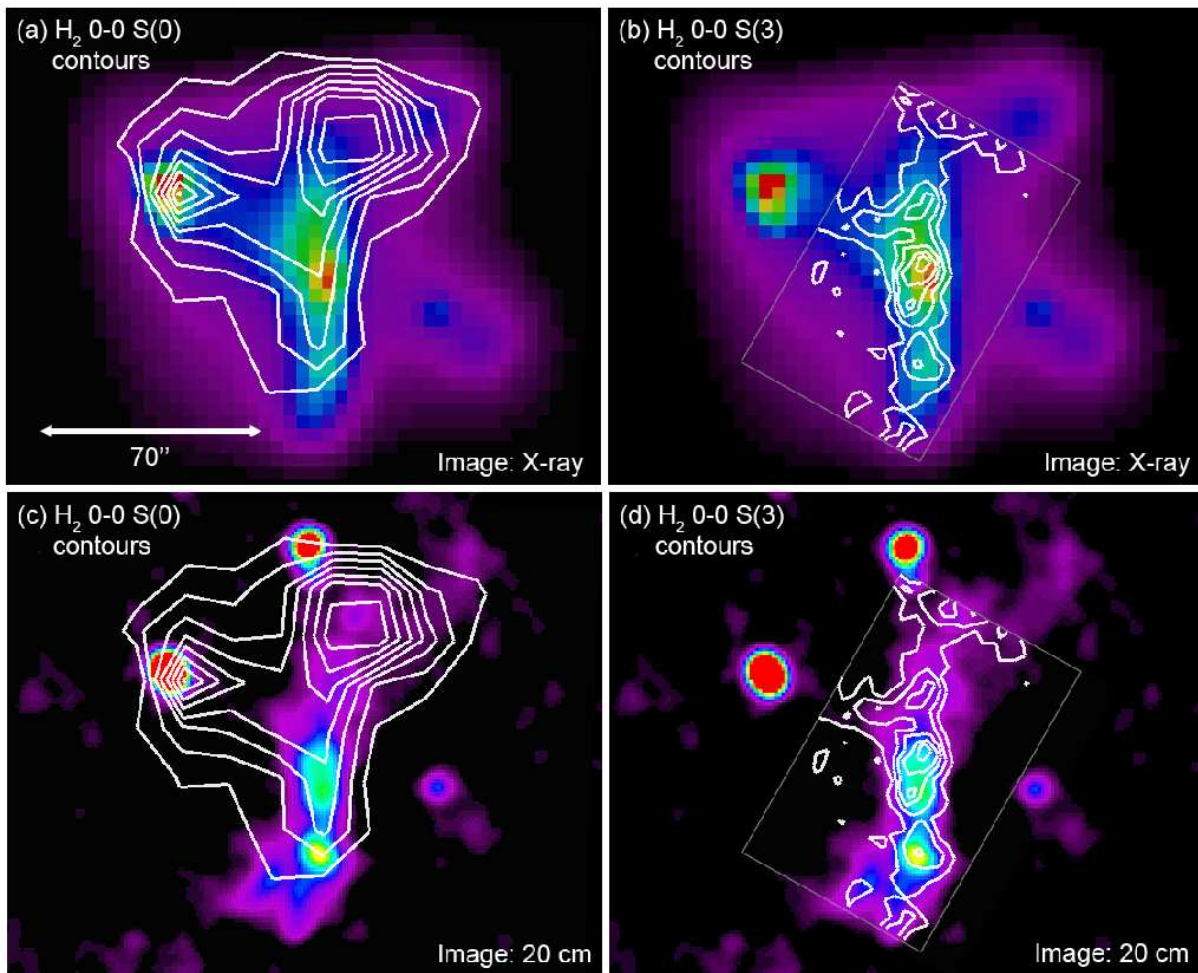
FIG. 3.— X-ray image from XMM-Newton (Trinchieri et al. 2005) in the 1.5−2.5 keV band with (a) H$_2$ S(0) contours and (b) H$_2$ S(3) contours overlaid. Also shown are 1.4 GHz radio continuum images from the VLA (Xu et al. 2003) with (c) H$_2$ S(0) contours and (d) H$_2$ S(3) contours overlaid. Contours levels are as in Fig 2.

complex, we detect faint emission from [Fe II]25.99μm at the location of the center of the shock (as defined by the X-ray "hotspot" in Fig. 3a). The energetic requirements for shocks to produce strong [Fe II] emission are usually present in J shocks while the ion abundance in C shocks are low in comparison (Hollenbach & McKee 1989). We will discuss the production of [Fe II] in the shock in Section 6.2.

The [S III]33.48μm distribution is presented in Figure 4b. This fine structure line acts as a strong tracer of H II regions (Dale et al. 2006) and we observe emission from SQ-A and from other regions of star formation in the South (see Section 3.3). In the primary shock region the distributions of [Fe II] and [S III] are anti-correlated.

In strong contrast to the weak [Fe II] emission, there is copious [Si II]34.82μm emission (Fig. 4c), which follows the S(1) distribution closely with respect to the primary shock, as mapped by X-ray emission (Fig. 4d).

Although [Si II] is commonly found in normal H II regions, we will demonstrate below that, apart from in SQ-A, the strong silicon emission does not correlate with regions of strong PAH emission (tracing star formation) in SQ, but instead closely follows the H$_2$ and X-ray (shock) distributions. [Si II] acts as an efficient coolant of X-ray-irradiated gas and is predicted to be one of the top four cooling lines under these circumstances (Maloney et al. 1996). We will discuss the excitation of [Si II] in the shock in Section 6.2.

[Ne II]12.81μm (with an ionisation potential of 21.6 eV) is also represented in the shock, as shown in Figure 5a, although it is also emitted from some H II regions associated with star formation, such as SQ-A and the star-forming region South of NGC 7318b (see Section 3.3). The [Ne III]15.56μm contours (with an ionisation potential of 41 eV) are shown in Figure 5b and are associated with excitation in the shock, as well as from regions of star formation (see Section 3.3). The higher ionisation line of [Ne III] is much weaker in the shock ridge, but regions of emission correspond closely to peaks seen for the H$_2$ S(3) line. The [Ne II] emission, however, exhibits clearly extended emission with regions of greatest luminosity matching those seen for the H$_2$ S(3) line. The [Ne II] emission suggests excitation from the shock, with [Ne III] found at the location of the center of the shock, similar to what is observed for [Fe II].

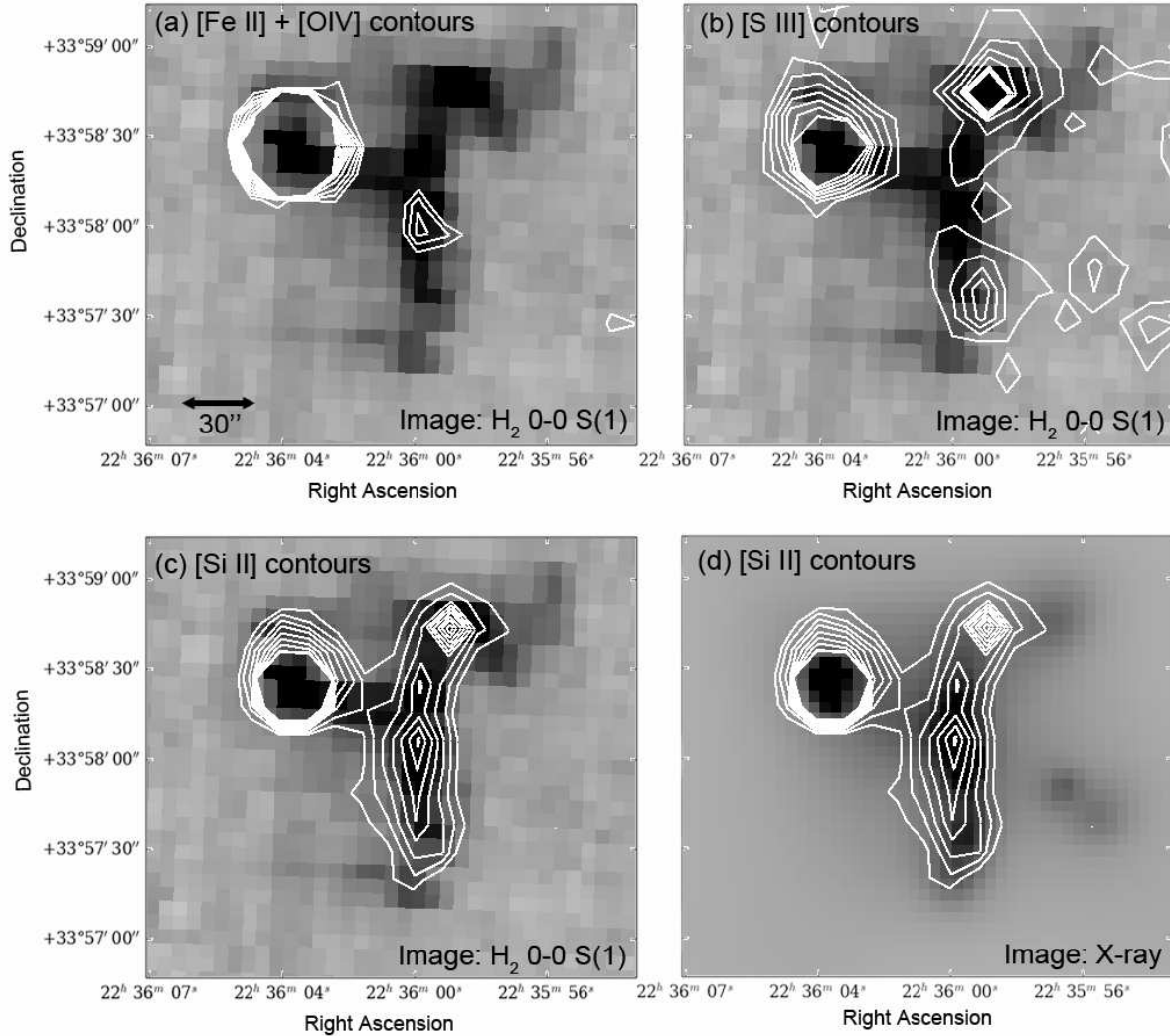### 3.3. Star Formation Tracers and Dust Emission in Stephan's Quintet

FIG. 4.— Fine structure emission ([Fe II]25.99μm and [O IV]25.89μm blend, [S III]33.48μm and [Si II]34.82μm) compared to the distribution of H$_2$ S(1) emission. Also shown are [Si II]34.82μm contours compared to X-ray 0.5-1.5 keV emission. Contour levels are as follows (all in units of MJy/sr): (a) 0.08, 0.1, 0.13, 0.15, 0.165, 0.18, 0.2, 0.22, 0.23, 0.25, (b) 0.2, 0.33, 0.47, 0.6, 0.73, 0.87, 1.0 with (c) and (d) having levels of 0.5, 0.66, 0.83, 0.99, 1.15, 1.31, 1.48, 1.6, 1.8. These levels are chosen to best show intensity of emission associated with the shock and do not reflect the full intensity range for NGC 7319.

Previous observations and spectroscopy of SQ (Xu et al. 2005) have determined that there are some regions of star formation associated with the spiral arms of the intruder galaxy NGC 7318b. We discuss in this section how these regions, which have a different spatial distribution from the shocked gas, are correlated with the PAH emission we detect in the IRS spectra.

In Figure 6a there is a strong correlation between the 11.3μm PAH distribution (from the IRS cube) superimposed on a Near-UV image from *Galex* (Xu et al. 2005), which maps the UV emission from hot stars associated with weak star formation from the system. This correlation suggests that the PAH molecules are excited by star formation. A similar close correlation is shown in Figure 6b where we overlay the 11.3μm contours on the IRAC 8μm band, which is dominated by the 7.7 and 8.6 μm feature. It is noticeable, however, that regions with strong 11.3μm emission in the shock, do not appear similarly strong at 8μm. This point will be addressed in Section 6.4.

We compare the 11.3μm PAH map to the distribution of warm dust in Figure 6c, using the MIPS 24μm map of SQ. Again, it is clear that there is a good correlation between the PAH emission and the thermal dust, most of which seems only poorly correlated with the shock ridge. The lack of conspicuous star formation in the ridge was also observed by Xu et al. (2003).

The main point we emphasize here is that the dust, PAH and UV emission appears to be associated with previously known star formation regions and no additional star formation is observed in the shock; this can be seen in Figure 6d showing the H$_2$ 0-0 S(1) emission overlaid on an IRAC 8μm image. There is little correspondence between the H$_2$ emission in the shock and 8μm (hot dust plus PAH) image. This is important because it implies that there is very little triggered star formation in the molecular gas associated with the shock-excited H$_2$.
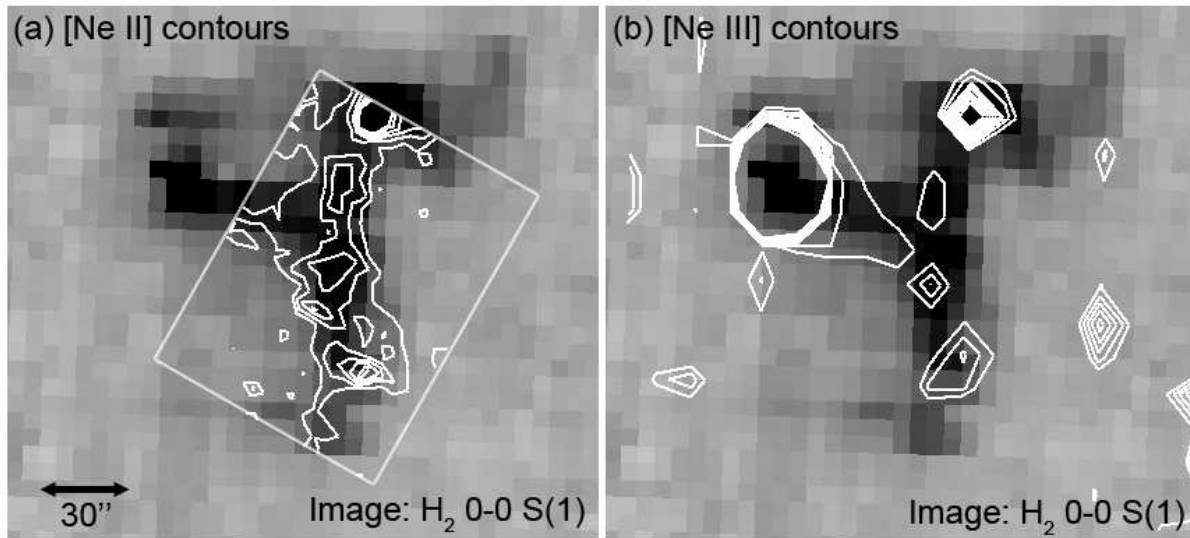
Figure 6c demonstrates that there is only faint dust

FIG. 5.— [Ne II]12.81μm and [Ne III]15.56μm emission compared to the distribution of H₂ S(1) emission. Contour levels are as follows (in units of MJy/sr): (a) 0.22, 0.4, 0.57, 0.75, 0.92, 1.1 and (b) 0.06, 0.08, 0.1, 0.13, 0.16, 0.18, 0.2, 0.23, 0.25.

emission at 24μm from the shock ridge. The presence of dust in the shock is required in the model of Guillard et al. (2009) to explain the formation of H₂ behind the shock and we do observe evidence of depletion onto dust grains (see Section 6.2). Thus the faint 24μm emission could be the result of destruction of Very Small Grains (VSGs), with only larger grains surviving, or indicate that the grains are cold and radiating more strongly at longer wavelengths, where *Spitzer* has the least spatial resolution. A more detailed description of the dust and faint PAH emission in the SQ group (including results from MIPS 70μm imaging) is discussed in separate papers (Guillard et al. 2010.; Natale et al. 2009, in preparation). Guillard et al. (2010) show that the IR emission in the shock is faint due to dust being heated by a relatively low intensity UV radiation field and determine a Galactic PAH/VSG abundance ratio in this region.

A more complete understanding of the likely existence of cool dust in the shock will require higher angular resolution and a broader wavelength coverage than that achieved by *Spitzer*.

Despite the faintness of emission from the main shock, the 24μm map presents a new result, which was less obvious in previous studies, namely that the dominant regions of star formation in SQ lie not in the galaxies themselves, but in two strikingly powerful, almost symmetrically disposed regions at either end of the shock. The region to the North is the well studied SQ-A, but the region to the South (which we refer to as 7318b-south) is also very powerful and both regions lie at the ends of the shock, as defined by the H₂ distribution. This may not be a coincidence, and we will discuss this further in Section 6.1.

The [Ne II]12.81μm, [Ne III]15.56μm and [S III]33.48μm fine-structure lines, as mentioned above, are also tracers of star formation in SQ as these lines are often associated with H II regions. The [Ne II]12.81μm emission appears to follow *both* the H₂ and the star formation regions (see Fig. 5a), appearing more extended in the South than the corresponding H₂ emission and flaring out where star

formation regions, especially 7318b-south, are observed optically, and through PAH emission (see Fig. 6).

4. GLOBAL PROPERTIES OF THE MOLECULAR HYDROGEN IN SQ

The warm molecular hydrogen in Stephan's Quintet follows the X-ray distribution in the main shock and in the "bridge" structure. This might suggest that the molecular hydrogen is excited directly by the X-ray heating. However, we will show that the H₂ emission exceeds by at least a factor of 3 the X-ray luminosity from the various shocked filaments, thus ruling out direct X-ray excitation from the shock.

To measure the strength of the H₂ emission, we extract spectra from various rectangular sub-areas of SQ which are defined in Figure 7. The spectra were extracted from CUBISM cubes built from each IRS module, and joined to make a continous spectrum–no scaling was necessary to join the spectra.

Figures 7 a, b and c indicate the spectral extraction regions of the main NS shock, a sub-region of the shock and a characteristic part of the "bridge". The shock sub-region is chosen to be just North of the center of the shock, avoiding regions contaminated by star formation in the intruder. Spectra for these extractions are shown in Figure 8 a, b and c. All three spectra, share the common property that they are dominated by molecular hydrogen emission. The shock sub-region (Fig. 8b), unlike Figure 8a, is less contaminated by the star forming regions discussed in the previous section. The MIR continuum of the main shock appears stronger than the shock sub-region indicating stronger emission from warm dust; this is likely the result of contamination from starforming regions in the main shock extraction. The bridge exhibits a similarly weak continuum emission compared to the shock sub-region.

Figure 8b includes photometry from the IRAC bands, 16μm Peak-up Image (PUI) and MIPS-24μm image superimposed on the IRS spectrum. These are useful to probe conditions in the shock, in particular star forma-
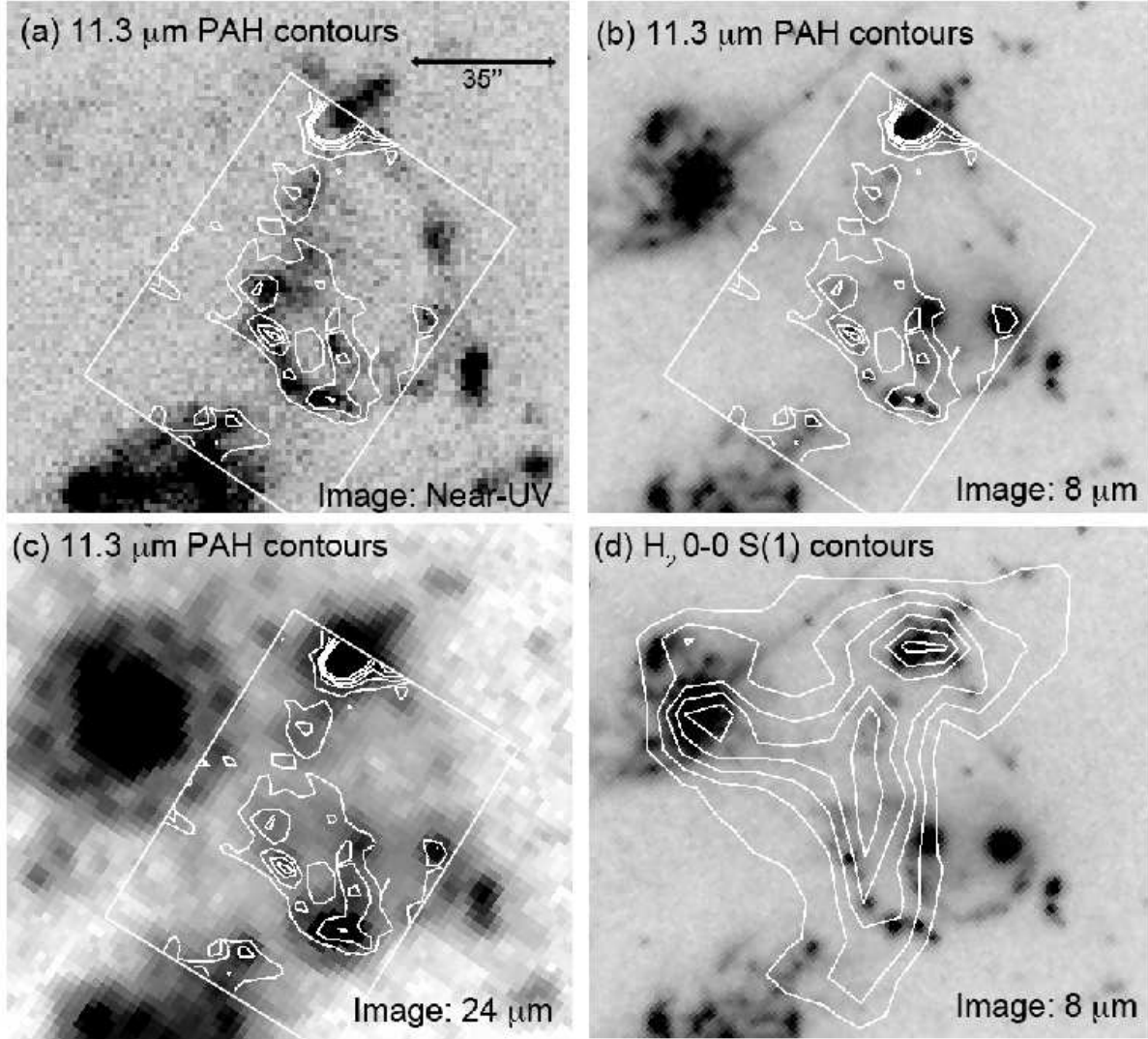
FIG. 6.— Dust as tracers of star formation. The 11.3μm PAH contours overlaid on (a) the Near-UV, (b) an 8μm image and (c) a 24μm image. By comparison the H₂ 0-0 S(1) contours show little correlation with the 8μm image (as shown in d). Contour levels are as follows (in units of MJy/sr): (a), (b) and (c) are 0.2, 0.35, 0.5, 0.65, 0.8. Contour levels for (d) are as in Fig. 2b.
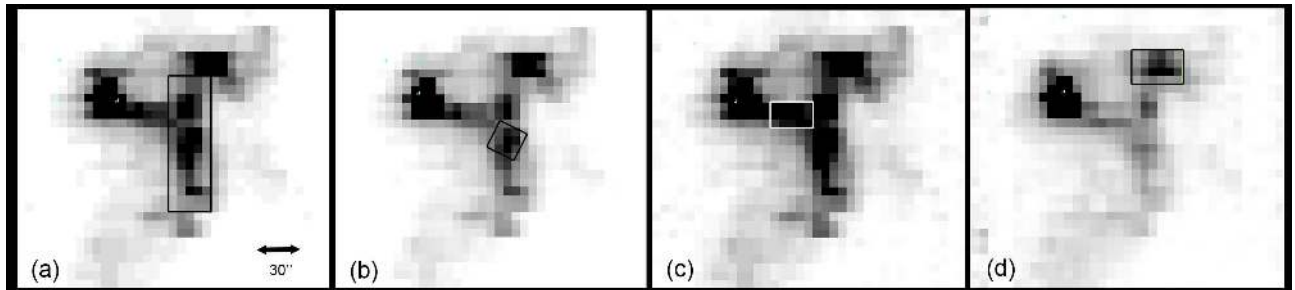
FIG. 7.— The rectangular sub-regions extracted from the main components of the SQ shock system overlaid on the H₂ 0-0 S(1) line emission. a) The Main Shock region centered on $22^h35^m59.6^s$, $+33°58'05.7''$. b) A region in the main shock centered on $22^h35^m59.97^s$, $+33°58'23.3''$ and chosen to have limited contamination from star forming regions in SQ. c) Extraction of the H₂ "bridge" feature centered on $22^h36^m0.14^s$, $+33°58'23.3''$. d) An extraction of the SQ-A star forming region centered on $22^h35^m58.85^s$, $+33°58'50.4''$.

(a) Main Shock Region

(b) Shock Sub-region

(c) "Bridge"

(d) SQ-A

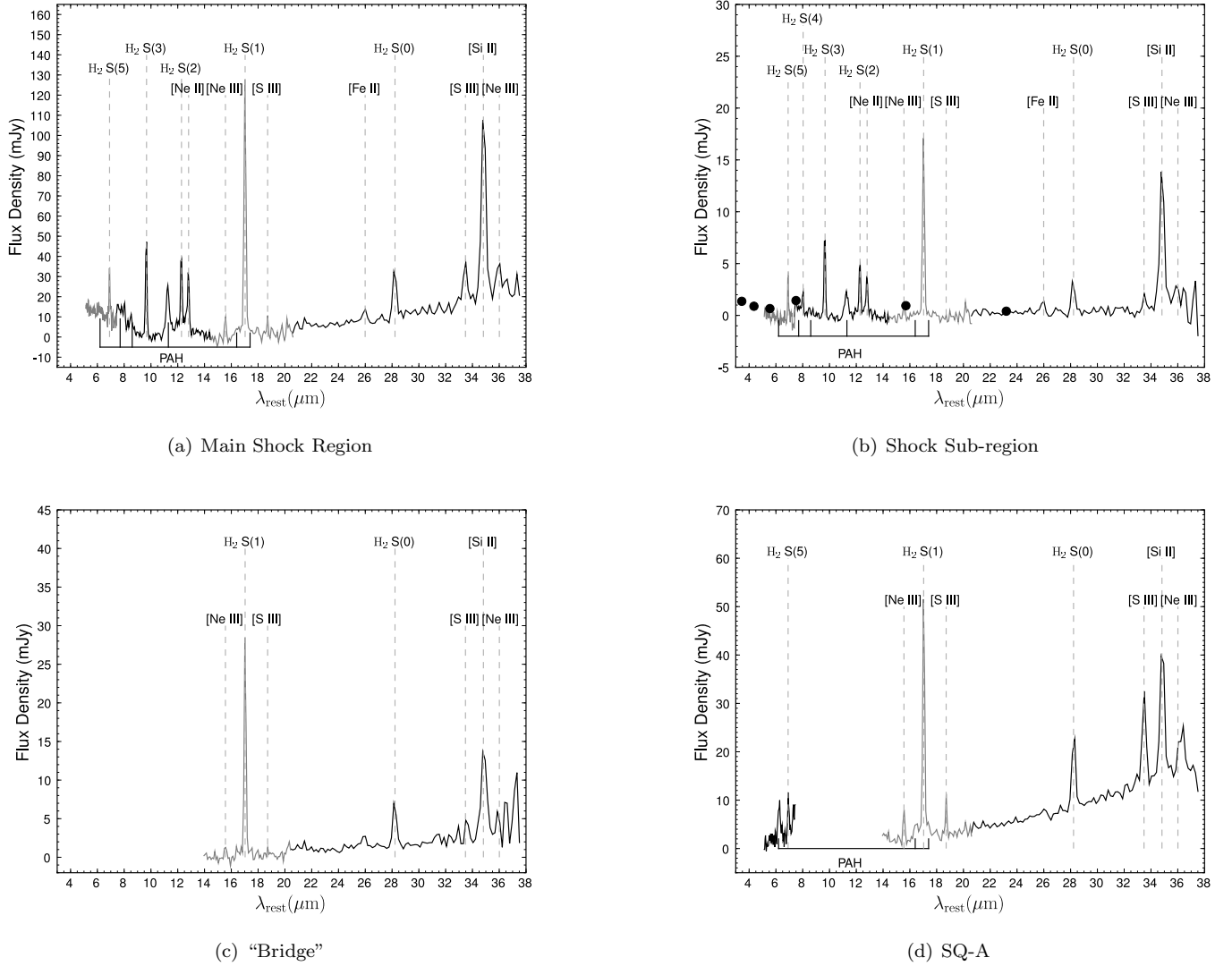FIG. 8.— Extracted Spectra (low resolution) of the regions shown in Figure 7, combining all IRS modules with coverage. The key emission features are labeled with measurements and sizes of extraction areas given in Table 2, which provides the H_2 line fluxes, and Table 3 listing the metal line measurements. The shock sub-region (shown in b) includes the IRAC, 16μm PUI and 24μm MIPS measurements for the same area. The 16μm flux is 0.939 ± 0.047 mJy, which includes emission from the 17.03μm H_2 line covered by the filter, while the 24μm flux is 0.408 ± 0.046 mJy; photometry was performed using a circular aperture with no aperture correction applied to compensate for contamination from the surrounding emission. The corresponding IRAC fluxes are 1.362 ± 0.068, 0.885 ± 0.045, 0.659 ± 0.036 and 1.434 ± 0.073 mJy for the 3.6, 4.5, 5.8 and 8.0 μm bands, respectively. The extraction of SQ-A (shown in d) also has coverage from the SL2 module due to the orientation of the IRS during the SL1 observation.

tion (see Section 6.4). Stellar light in the extraction area, from an extended spiral arm of NGC 7318b, produces contamination of the shock spectrum, visible as continuum emission shortwards of 6μm, in both Figure 8a and b.

There exists a striking similarity between the mid-IR spectrum of all three regions, showing powerful H$_2$ lines and low excitation weak emission from fine structure lines. Also the PAH emission observed in the spectra of the shock regions, and in the region of the "bridge" in the IRAC 8μm image (Fig. 6b), appears weak. This confirms that these properties, observed in the Appleton et al. (2006) observations of the shock core, extend to both the full extent of the main shock and the "bridge". This, and the fact that the "bridge" has similar X-ray properties to the main shock (see later) suggests that the bridge is a "scaled-down" version of the main shock. The weaker radio continuum emission at this location is significant. One possibility, that the "bridge" is older than the main shock, and the cosmic rays compressed in it have diffused away, will be discussed further in Paper II.Thus the new IRS observations seem to suggest that more than one large-scale group-wide shock is present in the group. This could be the result of previous tidal interactions and imply multiple shock heating events have taken place in SQ, consistent with what is seen in the X-ray (O'Sullivan et al. 2009).

Figures 7d and 8d present the extraction region and spectrum of SQ-A, the extragalactic star-forming region. In this case, although H$_2$ lines are still strong, a rising continuum and an increase in the strength of the metal lines relative to the H$_2$ is consistent with a spectrum that is increasingly dominated by star formation – a result which is already known from previous optical observations (Xu et al. 2003).

Line fluxes for all the H$_2$ and metal lines in the spectra discussed above are presented in Table 2 and Table 3, respectively. We estimate the luminosity emitted from the H$_2$ lines in the main aperture shown in Figure 8a. The emission from the 0-0 S(1) line alone can be calculated from Table 2 (for D = 94 Mpc) to be 2.3 $\times 10^{41}$ erg s^{-1}. Summing the emission measured in the observed lines for the main shock (0-0 S(0) through S(5) lines) and including an extra 28% emission from unobserved lines (see model fit to excitation diagram below), yields a total H$_2$ line luminosity from the main shock of 9.7 $\times 10^{41}$ erg s^{-1}. This phenomenal power in the molecular hydrogen lines dwarfs by a factor of ten the next brightest mid-IR line, which is [Si II]34.82μm with a line luminosity of L$_{SiII}$ = 0.85 $\times 10^{41}$ erg s^{-1}.

Figure 9 presents the excitation diagram of the low-J 0-0 H$_2$ transitions for the main shock extraction. The points are well fit by a model including three temperature components (T$_1$ = 158$\pm$6 K, T$_2$ = 412$\pm$4 K, and T$_3$ = 1500$\pm$200 K). It is likely that in reality, many different temperature components are present in the shock, and the three-temperature fit is only an approximation. However, it does allow us to provide an estimate of the total mass of warm H$_2$ of 5.0$\pm$1$\times 10^8$ M$_\odot$. Temperature T$_2$ is more uncertain than formally represented by the fit because it depends on the value of the S(4) flux, which may be systematically too low due to PAH contamination (see Fig. 9). In Paper II we will present a more com-

plete two-dimensional map of the excitation of the H$_2$ in SQ and explore variations in the shape of the excitation diagram along and across the shock in more detail.

Our observations have shown that H$_2$ is the dominant line coolant in the MIR. However, how does it compare with the most important coolant in high-speed shocks– namely the X-ray emission? Appleton et al. (2006) suggested that the H$_2$ emission was stronger than the X-ray emission at the shock center. This can now be evaluated over much of the inner SQ group.

We present a complete reanalysis of the XMM-Newton observations of SQ using the latest calibrations (see Appendix C for full details) in order to determine the fluxes and luminosities of the X-ray emission to match our spectral extractions. The results indicate the striking dominance of the H$_2$ line luminosities compared with the X-ray emission from the same regions. For the main shock, the X-ray "Bolometric" flux of L$_{X(0.001-10\text{keV})}$ = 2.8 $\times$ 10^{-13}erg s^{-1}cm^{-2} corresponds to 2.95 $\times$ 10^{41} erg s^{-1}, or L(H$_2$)/L$_{X(0.001-10\text{keV})}$ = 2.9. This is a lower limit since we have not attempted to remove the contribution to the main shock aperture of an extended group-wide X-ray component upon which the emission from the shock lies. Therefore it is likely that the H$_2$ line luminosity dominates over the main shock X-ray gas by a factor $\geq$ 3. Similar calculations can be done for the other regions for which H$_2$ spectra have been extracted. For example, in the "bridge" region, which we have already indicated has many of the same characteristics as the main shock, we find L(H$_2$)/L$_{X(0.001-10\text{keV})}$ = 2.5. These values demonstrate that throughout the extended regions of SQ, the molecular hydrogen cooling pathway dominates over the X-ray in this shocked system. This is a very significant result, upturning the traditional view that X-ray emission always dominates cooling in the later stages of evolution in compact groups of galaxies.

5. EMISSION LINE DIAGNOSTICS

The fine-structure flux ratios (see Table 3) can be used to probe the conditions within the extracted regions of SQ. The [Si II] 34.82μm/[S III]33.48μm ratio provides an indication of the sources of excitation within the system. As mentioned previously, [S III] is mainly a tracer of H II regions, whereas enhanced [Si II] emission can be generated via several mechanisms, including thermal excitation by X-rays (XDRs), or in shocks. In the main shock, the [Si II] 34.82μm/[S III]33.48μm ratio of $\sim$ 4.59 is high compared to, for example, both normal galaxies ($\sim$ 1.2) and AGN ($\sim$ 2.9) in the SINGS sample (Dale et al. 2006). However, this large aperture is contaminated by star formation emission from SQ-A and the intruder galaxy. A better measure is given by the smaller shock sub-region, where the [Si II] 34.82μm/[S III]33.48μm ratio is $\sim$ 9.5. Thus it is clear that the [Si II] emission is well outside the normal range of values, even for local well-studied AGN. Using the upper limit found for [S III] 33.48μm in the "bridge" structure, we find a ratio of $>$ 5 – again values well outside the range of normal galaxy disk emission. Indeed, these high values are typical of galactic supernova remnants where shock excitation is well determined (e.g. Neufeld et al. 2007; Hewitt et al. 2009). We will argue in the next section that silicon is being ionised in regions experiencing fast
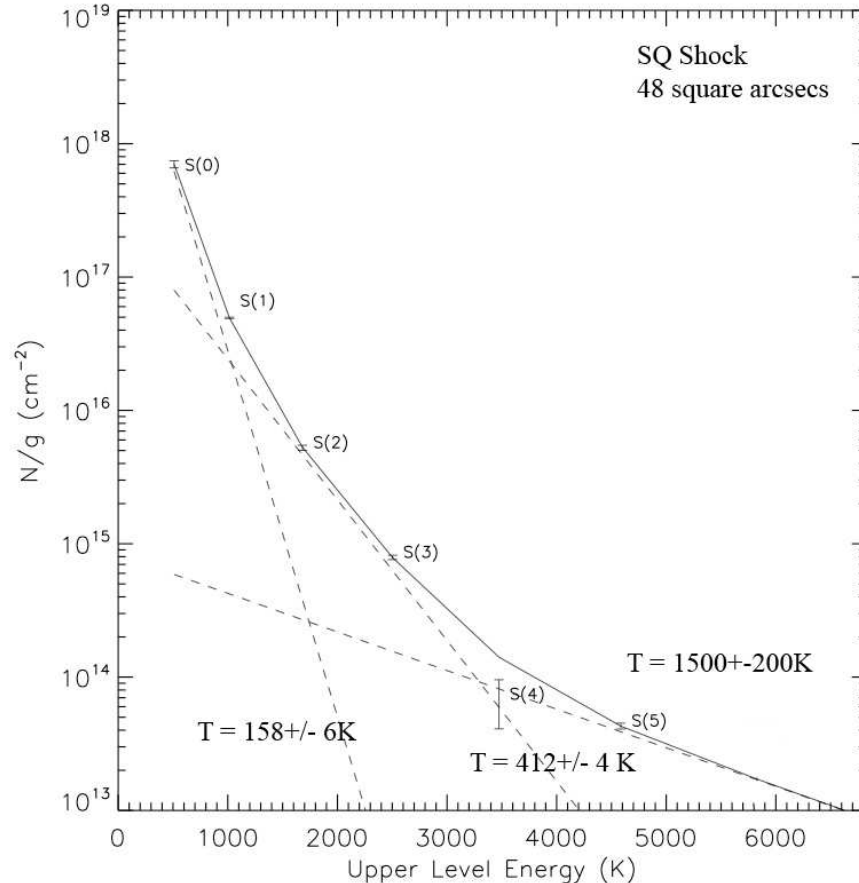
FIG. 9.— Excitation Diagram of the Main Shock region in Stephan's Quintet. The ordinate (N/g) represents the column density divided by the statistical weight of the rotational state.

shocks $100 < V_s < 300 \, \text{km s}^{-1}$ and depleted onto dust grains. The [Fe II] 26.0μm/[Si II] 34.82μm ratio for the main shock and sub-region (~ 0.12) is in agreement with values found by Neufeld et al. (2007) for their sample of SNR.

For the extragalactic star forming region SQ-A, [Si II] 34.82μm/[S III] 33.48μm is $\sim$1.49, only slightly higher than the average of ~ 1.2 found for star-forming regions in the SINGS sample (Dale et al. 2006); another indication that SQ-A is dominated by star formation.

In star-forming galaxies the [Ne III] 15.56μm/[Ne II] 12.81μm ratio can be used as a measure of the hardness of the radiation field as it is sensitive to the effective temperature of the ionising sources. In the main shock, we find a value of ~ 0.36 which would be considered typical compared to those found in starburst systems, which range from $\sim 0.03 - 15$ (Verma et al. 2003; Bernard-Salas et al. 2009), and in supernovae remnants ranging from $\sim 0.07 - 1.24$ (Neufeld et al. 2007; Hewitt et al. 2009). The shock subregion has a ratio of only ~ 0.14 indicating a lower intensity radiation field North of the shock center. However, it is clear from its spatial distribution relative to the 8μm and H$_2$ emission, that most of the neon is not originating from star formation, and so shocks are an obvious source of excitation.

The [Ne II] 12.81μm/[Ne III] 15.56μm ratio can be used

to estimate the shock velocity using the MAPPINGS shock model library of Allen et al. (2008). In the main shock this ratio corresponds to shock speeds of between 100 and $300 \, \text{km s}^{-1}$ (using preshock densities of $0.01 < n < 100 \, \text{cm}^{-3}$ and magnetic parameter $B/n^{0.5}$ = 1 and 3.23 – the nominal equipartition value[11]). We do, however, have contamination from starforming regions in the main shock and cannot disentangle this emission from that produced in the shock. To address this we use the [Ne II] 12.81μm and [Ne III] 15.56μm maps to mask areas associated with star formation (see Section 3.3) and determine a lower limit for the [Ne II] 12.81μm/[Ne III] 15.56μm ratio in the shock of ~ 4.54. This value corresponds to a shock velocity of $\sim 150 \, \text{km s}^{-1}$.

The average electron density is determined from the [S III]18.71μm/[S III]33.48μm (two lines of the same ionisation state) ratio. For SQ-A we find a ratio of $\sim$0.56, and in the main shock $\sim$0.41. This corresponds to an electron density of $100 - 200 \, \text{cm}^{-3}$ (Martín-Hernández et al. 2002) for both, i.e. in the low-density limit for this diagnostic (Smith et al. 2009).

6. THE GROUP-WIDE SHOCKS

6.1. Origin of the H$_2$ and X-ray emission

[11] See Allen et al.(2008)

Our observations have shown that the molecular hydrogen and X-ray emitting plasma appear to follow a similar distribution, and we have ruled out the possibility that this is a consequence of X-rays heating the H_2, since the H_2 has the dominant luminosity. How then can we explain the similar distributions? Are these results consistent with the hypothesis that the shock is formed where the intruding galaxy NGC 7318b collides with a pre-existing tidal filament of H I drawn out of NGC 7319 in a previous interaction with another group member (Moles et al. 1997; Trinchieri et al. 2003)?

This basic mechanical picture appears plausible as can be seen in Figure 10 which shows that the H_2 distribution "fills in" the gap in the H I tidal tail as observed by the VLA (Williams et al. 2002). The implication is that the H I has been converted into both a hot X-ray component and a warm H_2 component by the collision of the intruder with the now missing H I.

Part of the puzzle of how this high-speed ($V_s \sim 700 - 1000$ km s^{-1}) shock can lead to both X-ray and very strong molecular line emission is presented in a model by Guillard et al. (2009). The high-speed collision of NGC 7318b with the H I filament (assumed to be composed of a multiphase medium) leads to multiple shocks passing through and compressing denser clumps (which become dusty nucleation sites for H_2 formation) as opposed to the lower-density gas, which is shock-heated to X-ray temperatures. The H_2 therefore forms in denser clouds experiencing slower shocks. Thus the coexistence of both hot X-ray gas, and cooler molecular material is a natural consequence of the multiphase medium of the pre-shocked material.

Modeling of the H_2 excitation by Guillard et al. (2009) demonstrates that the emission can be reproduced by low velocity ($\sim 5 - 20$ km s^{-1}) magnetohydrodynamic shocks within the dense ($n_H > 10^3$ cm^{-3}) H_2 gas. The denser clouds survive long enough to be heated by turbulence in the hot-gas component, tapping into the large available kinetic energy of the shock. This picture is consistent with both the broad H_2 linewidth (870 km s^{-1}) measured in IRS high-resolution spectrometer observations of Appleton et al. (2006), and the velocity center of the warm H_2 (based on new IRS spectral calibrations - see Appendix B) which places the gas at intermediate velocities between the intruder and the group IGM. Both these measurements are consistent with H_2 being accelerated in a turbulent post-shocked layer.

Intermediate pre-shock densities and post-shock temperatures result in regions of H I and H II that have cooled, but where the dust content has been destroyed (Guillard et al. 2009). Pre-existing Giant Molecular Clouds (GMCs) which may have been embedded in the H I gas, would be rapidly compressed and collapse quickly, thus forming stars. This mechanism, proposed for SQ-A by Xu et al. (2003), might also apply to 7318b-south. However, if this was the case, it would have to explain why two such GMCs happened to be positioned at the extreme ends of the current shock – an unlikely coincidence. More probable, however, is that the geometry of the shock somehow favors the collapse of clouds at the ends of the shock – perhaps in regions where the turbulent heating is less efficient.

6.2. Origin of [Fe II] and [Si II] emission

As outlined above, the combination of emission detected in the shock region of SQ can be understood in terms of a spectrum of shock velocities. The fastest shock velocities ($V_s \sim 600$ km s^{-1}) are associated with the lowest density pre-shock regions and the post-shock X-ray emitting plasma. These are fast J shocks and represent a discontinuous change of hydrodynamic variables and are often dissociative (Hollenbach & McKee 1989). C shocks have a broad transition region such that the transition from pre-shock to post-shock is continuous and are usually non-dissociative (Draine et al. 1983). The lowest velocity shocks associated with the turbulent H_2 emission are $\sim 5 - 20$ km s^{-1} C shocks (Guillard et al. 2009). Xu et al. (2003) find optical emission line ratios consistent with shock models that do not include a radiative precursor (Dopita & Sutherland 1995).

The [Fe II]25.99μm emission associated with the shock region in SQ is relatively weak, but coincides with the most energetic part of the shock as traced by the X-rays (Fig. 4). We also detect abundant [Si II]34.82μm emission associated with the main shock.

Silicon and iron have very similar first and second ionization potentials. Their first ionization potentials (7.9 and 8.15 eV for Fe and Si, respectively) are lower than that of hydrogen but their second ionization potential is higher (16.19 and 16.35 eV). The MIR [Fe II] and [Si II] line emission observed from the SQ shock could thus arise from predominantly neutral, as well as ionized gas. We discuss the contribution from the ionized gas using the [Fe II](25.99μm)/[Ne II](12.81μm) and [Si II](34.82μm)/[Ne II](12.81μm) line ratios. The high [Ne II](12.81μm)/[Ne III](15.56μm) mid-IR line ratio (see Section 5) implies that [Ne II] is the dominant ionization state of Ne in the SQ shock. Unlike Fe and Si, Ne is not much depleted on dust (Simpson et al. 1998). Because the [Ne II] 12.81μm line has a high critical density ($n_e = 4.3 \times 10^5$ cm^{-3}, Ho and Keto 2007), the neon line strength scales with the emission measure of the ionised gas.

The optical line emission from the SQ shock is discussed in detail in Xu et al. (2003). The high values of the [O I](6300Å) and [N II](6584Å) lines to Hα line ratios are evidence of shock ionization. The optical [S II](6716Å/6731Å) line ratio as well as the MIR [S III] line ratio correspond to the low density limit (see Section 5) and comparison with the shock models of Allen et al. (2008) constrain the pre-shock gas density to be about 1 cm^{-3} or smaller.

In Figure 11 we indicate the region (in grey) corresponding to the observed MIR ratios (using the upper and lower limits determined for the [Ne II]12.81μm line emission as discussed in Section 5). For comparison the expected emission from the shock models of Allen et al. (2008) are displayed for a pre-shock gas density of 1 cm^{-3} and two values of the magnetic parameter, $B/n^{0.5} = 0.5$ and 3. For clarity of the figure, only shock velocities from 100 to 300 km s^{-1} are used and higher velocities shocks which do not match the observed [Ne II]/[Ne III] line emission ratio (see Section 5) are discarded.

The observed [Fe II](25.99μm)/[Ne II](12.81μm) and [Si II](34.82μm)/[Ne II](12.81μm) ratios are both smaller than the shock values. The iron and silicon lines are
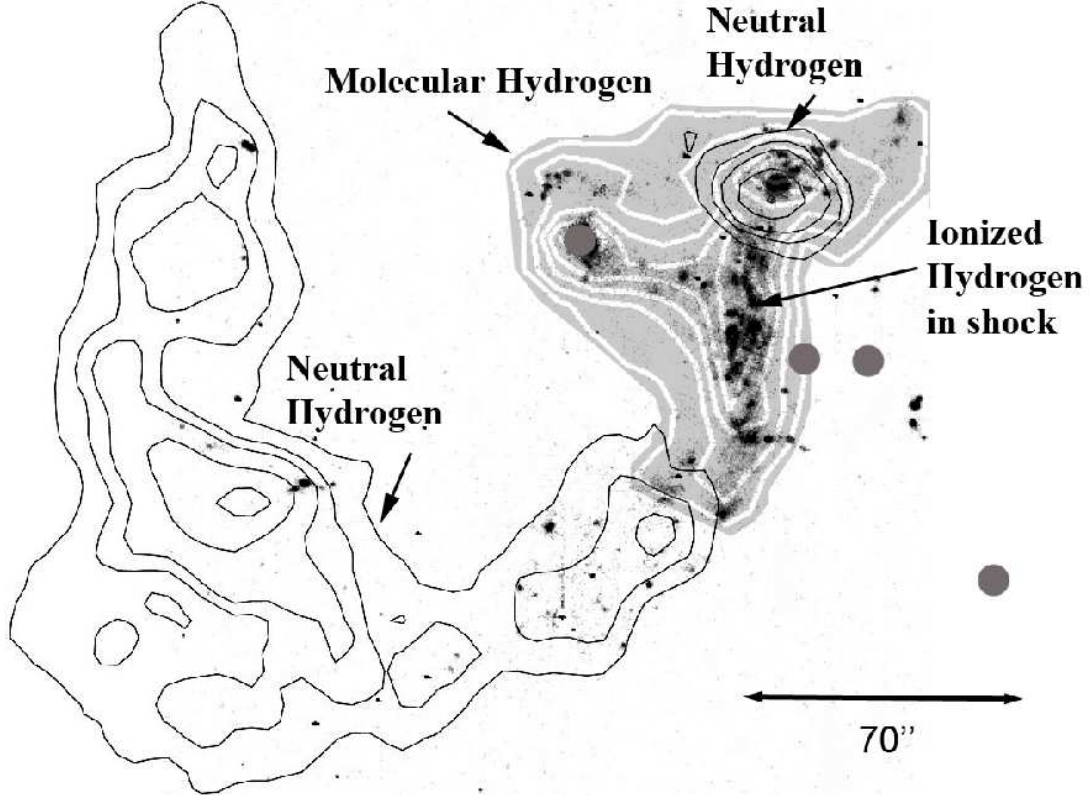
FIG. 10.— Schematic Diagram of the H I distribution in Stephan's Quintet, from Williams et al. (2002), and the H$_\alpha$ emission (Xu et al. 1999), with the H$_2$ 0-0 S(1) emission overlaid. The grey dots represent the locations of the core galaxies in the group as shown in Fig. 1.

not dominant cooling lines of ionizing shocks. The gas abundances of these elements do not impact the thermal structure of the shock and the line intensities roughly scale with the gas phase abundances. We thus interpret the offset between the IRS observation and model values as evidence for Fe and Si depletion. We consider the magnitude of the depletions indicated by the arrow ($\sim$50% and $\sim$60% for Fe and Si, respectively) in Figure 11 as lower limits since there could be a contribution to the [Fe II] and [Si II] line emission from non-ionizing J-shocks into molecular gas (Hollenbach & McKee 1989). Such shocks could also contribute to the [O I](6300Å) line emission as discussed in Guillard et al. (2009). Forthcoming observations of the H$_2$ ro-vibrational line emission in the near-IR should allow us to estimate whether they may be significant. A contribution from non-ionizing shocks to the [Fe II] and [Si II] line emission will raise the depletion of both Fe and Si as well as the Fe/Si depletion ratio because non-ionizing shocks do not produce [Ne II] line emission and the [Fe II](25.99μm)/[Si II](34.82μm) line emission ratio in J-shocks within dense gas is larger than for shocks plotted in Figure 11.

6.3. *Comparison with Cold H$_2$ Distribution*

A key aspect to understanding the emission we observe in SQ, as well as a test of the proposed model of H$_2$ excitation, is the amount and distribution of cold H$_2$, as measured by CO. A reservoir of cold H$_2$ associated with the warm gas observed in SQ would provide key insight into conditions within the intragroup medium. In Fig-

ure 12 we show the BIMA CO (1-0) integrated intensity contours from Gao & Xu (2000), shown with the H$_2$ S(0) and S(1) emission contours, overlaid on an optical image of SQ. These interferometric observations use the large primary beam of 110″, centered on the shock, to determine areas of high column densities in the group. The CO traces areas of known star formation seen at 24μm and in the NUV (see Section 3.3), notably SQ-A and 7318b-south. As observed by Yun et al. (1997), the CO around NGC 7319 is concentrated in two regions. The dominant complex is North of the nucleus residing in a dusty tidal feature. The nuclear CO is elongated perpendicular to the stellar disk suggesting a deficiency of ongoing star formation in the disk.

The CO distribution does not correlate with the location of warm H$_2$ emission, particularly around NGC 7319. The cold H$_2$ complexes are clearly offset from the concentrations of warm H$_2$. Even the S(0) emission line (see Fig. 12a), which follows the coldest warm H$_2$, does not have peaks corresponding to the strongest CO detections.

In a forthcoming paper (Guillard et al. 2010, in preparation), we will report the recent detection of ^{12}CO(1-0) and (2-1) emission, associated with the warm H$_2$ in the SQ shock, using the single-dish 30m IRAM telescope. These observations suggest that most of the CO emission in the shock has been missed by interferometers (because of the broad linewidth) and show that the CO emission is both present in the shock, and extends along the H$_2$-emitting bridge and towards NGC 7319.
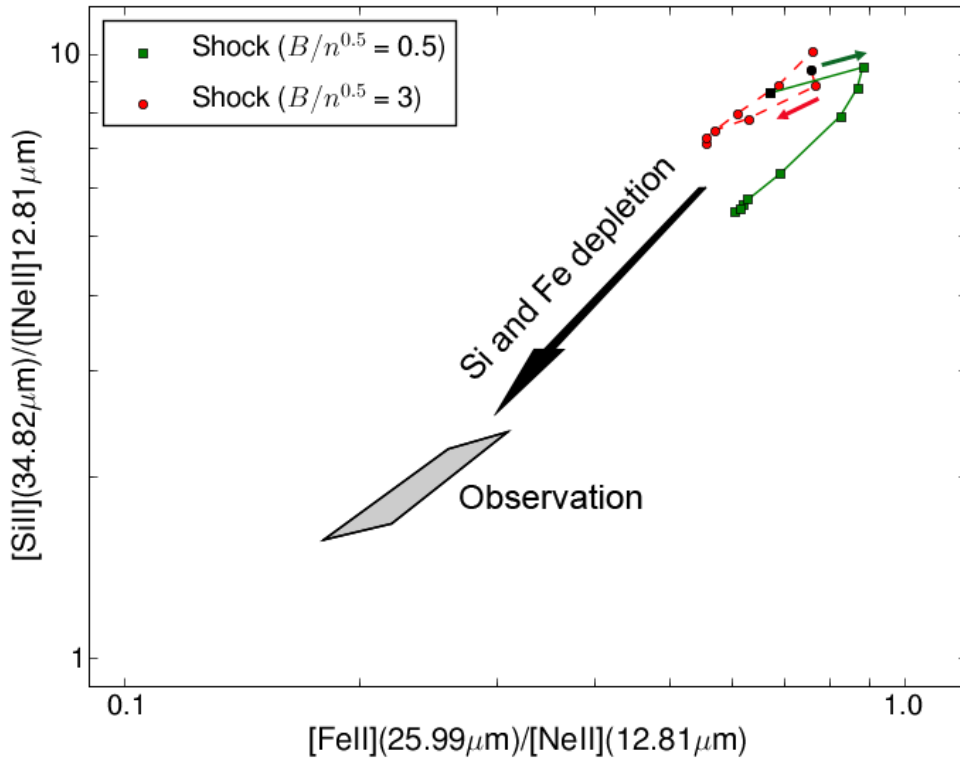
FIG. 11.— The line ratios measured in the Main SQ shock of the [Ne II](12.8μm), [Fe II](26.0μm), and [Si II](34.8μm) lines are compared with shock calculations from Allen et al. (2008). The model values cover a shock velocity range of $100-300$ km s^{-1} with a gas density of $1\,{\rm cm}^{-3}$ and two values of the magnetic parameter $B/n^{0.5} = 0.5$ (green square) and 3 (red circles). The black symbols represent the 100 km s^{-1} values and the arrows indicate the direction of increasing velocity (in steps of 25 km s^{-1}). The grey area indicates the range of line ratios, [Si II]/[Ne II] and [Fe II]/[Ne II], determined from observations (as discussed in Section 5). The ratios are lower than the model values which we interpret as evidence for Si and Fe depletion onto dust grains.
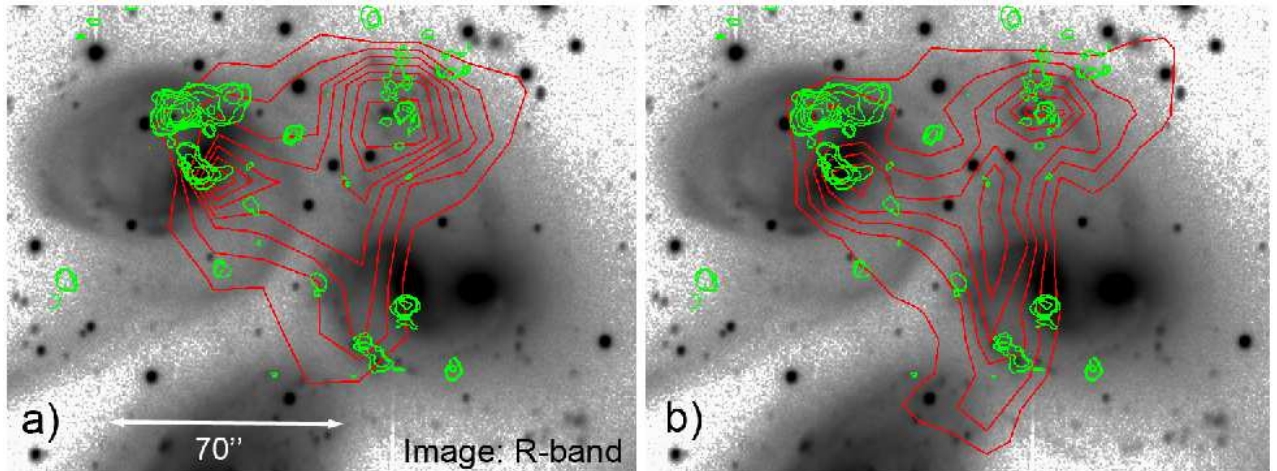
FIG. 12.— CO (1-0) contours (green) from Gao & Xu (2000) overliad on an R-band image (Xu et al. 1999) of the group. Contour levels correspond to 2.4σ, 3.0σ, 4.0σ, 5.0σ, 6.0σ, 7.0σ and 8σ (1.0σ $\sim$0.025 Jy). We show the H$_2$ contours (red) for the S(0) line (a) and the S(1) line (b) with contour levels as in Fig. 2a and b respectively.

The kinematics of the CO gas lying outside of star-forming regions, in the new observations, appears to be

highly disturbed with a broad linewidth in agreement with the Appleton et al. (2006) interpretation that the

MIR H_2 lines were intrinsically very broad and resolved by the high resolution module of IRS. The CO data also agrees with our re-analysis of the Appleton et al. (2006) data (see Appendix B) using more recent and reliable wavelength calibration, which places the bulk of the H_2 gas at velocities intermediate to that of the intruder and the group – supporting the idea that the H_2 gas is accelerated in the shock.

6.4. *Turbulent Suppression of Star Formation in the H_2 filaments*

Section 3.3 discussed the star forming regions observed in SQ and noted that there was very little evidence for star formation in the shock associated with the warm H_2 emission. The main shock contains a large quantity of warm molecular hydrogen ($5.0 \times 10^8\,\mathrm{M_\odot}$) providing a reservoir of fuel for star formation once it cools (see Section 4). We investigate star formation in the warm H_2-dominated medium by considering the shock sub-region, chosen to avoid star forming regions in the intruder galaxy, but likely still subject to some contamination from these regions.

PAH emission is a classical tracer of star formation, but the molecules are fragile and easily destroyed in hard radiation fields. In the spectra of the main shock and subregion (Fig. 8a and b) the PAH emission bands at 6.2 μm, 7.7 μm and 8.6 μm are far weaker compared to the 11.3 μm bands, which when strong are predominantly produced by neutral PAH molecules (Draine & Li 2001). In the shock subregion we find an upper limit flux for the 6.2 μm PAH of $0.47 \times 10^{-17}\,\mathrm{W\,m^{-2}}$ and fluxes of $0.87 \times 10^{-17}\,\mathrm{W\,m^{-2}}$ and $2.49 \times 10^{-17}\,\mathrm{W\,m^{-2}}$ for the 7.7 and 11.3 μm bands respectively. This corresponds to a 7.7μm/11.3μm PAH ratio of 0.35, very low compared to the median value found for the SINGS sample of 3.6 (Smith et al. 2007).

The suppression of the 7.7μm/11.3μm PAH ratio has been observed in AGN environments (e.g. low-luminosity AGN in the SINGS sample of Smith et al. 2007) and is favored to be the result of selective destruction of PAH molecules small enough to emit at 7.7μm. PAH processing in the shock due to larger molecules being less fragile than smaller ones is discussed further in Guillard et al. (2010). An alternative explanation is that the PAH molecules are chiefly large and neutral in the shock, producing enhanced 11.3μm emission in comparison to the smaller PAH molecules. A detailed comparison of the dust and PAH emission properties can be found in Guillard et al. (2010).

Dust emission in the mid- and far-infrared can be used to infer the amount of star formation taking place (Kennicutt 1998). We measure a 24μm flux in this region of 0.408 mJy, corresponding to a spectral luminosity (νL_ν) of $L_{24} = 1.38 \times 10^7 L_\odot$. This low luminosity is consistent with the weak MIR continuum (Fig. 8b), arising from emission from VSGs heated by the UV radiation field.

We can combine this with a measurement of the Hα emission in this region to obtain a star formation rate (SFR), given that they are complimentary (Hα tracing the young stellar population and 24μm as a measure of dust-absorbed stellar light). We find $L_{H\alpha} = 2.03 \times 10^6 L_\odot$, but caution that H$\alpha$ emission in SQ is also the result of shock-excitation (Xu et al. 2003) and must

be considered an upper limit for measuring star formation. When we combine $L_{H\alpha}$ with L_{24}, using the relation of Calzetti et al. (2007), we find a SFR of $<0.05\,M_\odot\,\mathrm{yr^{-1}}$.

A further measure of star formation can be obtained from the PAH strength. Using the relation of Houck et al. (2007), derived from the starburst sample of Brandl et al. (2006), we can use the 7.7μm flux density as a measure of star formation. The shock subregion has a 7.7μm flux density of 0.73 mJy which corresponds to a SFR of $\sim 0.08\,M_\odot\,\mathrm{yr^{-1}}$, in good agreement with our previous calculation, but also an upper limit as some PAH emission is contamination from known star formation regions in the group. A point of caution, however, is that this star formation indicator may be biased given that we detect suppressed 7.7μm emission compared to the 11.3μm PAH. Comparing the $L_{PAH}(7.7\mu m)/L_{24}$ ratio to the galaxies in SINGS, we find that the value of ~ 0.17 is typical of star-forming galaxies (Ogle et al. 2009), which suggests that both measures of star formation are low, but self-consistent.

The low *upper limits* for the SFR in the shock suggests that star formation is depressed in the shock apart from in the IGM starburst, SQ-A, which has a SFR of $\sim 1.25\,M_\odot\,\mathrm{yr^{-1}}$ at the velocity of the group (Xu et al. 2003). This would be consistent with a picture of molecular hydrogen being reheated by MHD shocks in the turbulent medium.

Since the Jeans' mass increases with gas temperature and turbulence and shearing morions will prevent collapse, the cold molecular gas clouds may be too short-lived or undersized to facilitate collapse and produce significant star formation (Guillard et al. 2009). The extent of a cold reservoir of molecular gas in the shock is a key consideration in this scenario, as discussed in Section 6.3.

7. IMPLICATIONS FOR HIGH-Z GALAXY FORMATION

The present observations suggest that molecular line cooling in dense clumps dissipates a significant fraction of the kinetic energy available in high-speed shocks. For reference, and to provide a glimpse of what this group might look like at high redshift when filling a single beam, we present in Figure 13 the spectrum extracted for the entire group (i.e. including the three neighboring galaxies and the shock). The total H_2 line emission from the whole group exceeds $10^{42}\,\mathrm{erg\,s^{-1}}$ and is still the most dominant MIR coolant. Indeed the luminosity of the rotational H_2 lines is sufficient that it could be detected at high redshift with future far-infrared or sub-mm instrumentation like SPICA or SAFIR (see Appleton et al. 2009). How likely is it, however, that high-speed shocks play a role in the assembly of galaxies?

There is growing evidence that galaxies at high redshift are turbulent (Förster Schreiber et al. 2006; Genzel et al. 2008) and increasingly clumpy (e.g. Conselice et al. 2005, Elmegreen & Elmegreen 2005). Indeed Bournaud & Elmegreen (2009) discuss the importance of the growth instabilities in massive gas clumps in forming disks at z > 1, and favor at least a large fraction of the clump systems being formed in smooth flows, perhaps similar to those discussed by Dekel et al. (2009). To what extent the build-up of these disks is truly "smooth" is not yet clear since the medium is likely to be a multiphase one. In a more standard picture, gas flowing into the more massive dark halos will experience strong
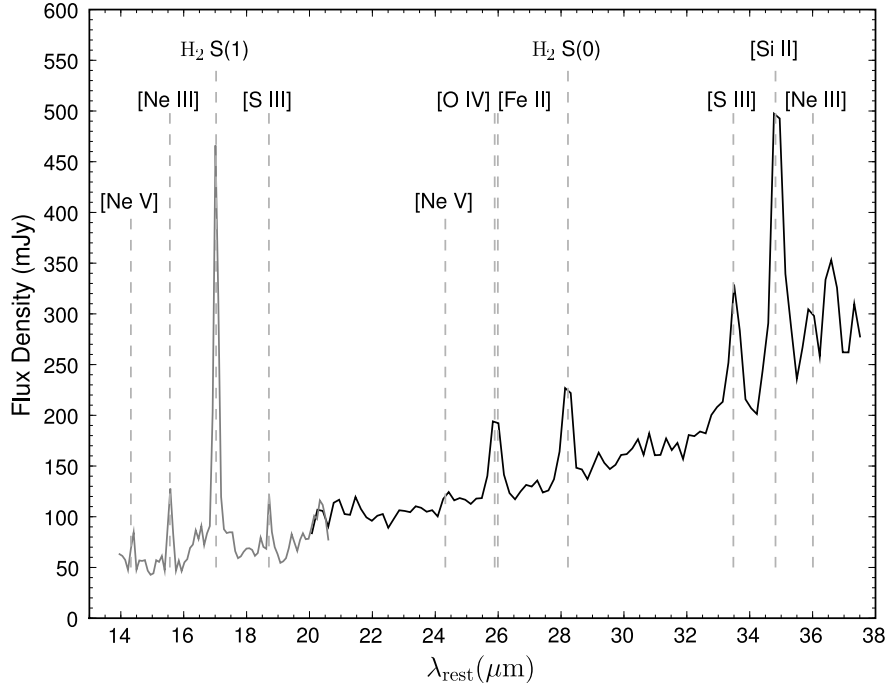
FIG. 13.— Low resolution spectrum of the entire SQ region mapped by the IRS. This extraction is a rectangular box corresponding to an area of 94 kpc × 56 kpc centered on $22^h35^m59.97^s$, $+33°58'12.7''$, and includes the main shock, H₂ bridge, NGC 7319, SQ-A and NGC 7318a and NGC 7318b.

shocks, most likely in an inhomogenious medium (e. g. Greif et al. 2008) – thus it begs the question of how important H₂ cooling may be in these different cases.

Models of the collapse of the first structures predict that strong metal lines soon dominate the cooling over molecular hydrogen when the first stars pollute the environment. It is therefore usually assumed that, except at very early stages, molecular hydrogen is a minority coolant in gas that forms the first major structures (e.g. Bromm et al. 2001, Santoro and Shull 2006). However, our observations show that, under the right conditions, even in high metallicity environments, molecular hydrogen can be extremely powerful – in this case dominating by a factor of ten over the usually powerful [Si II]34.82μm line in strong shocks. If there are situations at high redshift where strong shocks propagate into a clumpy, multiphase medium, then our observations imply that molecular hydrogen cooling cannot be assumed to be negligible. On the other hand, this will not be a trivial problem. Our best model of Stephan's Quintet (Guillard et al. 2009) involves the formation of H₂ in a complex multiphase turbulent medium in which shocks destroy dust in some places, but allow survival in others - thus encouraging H₂ formation.

In the early universe, this enhanced cooling, which has so far been neglected, will depend on the distribution and nature of the first dust grains, in concert with the formation, temperature and abundance of gas, and the feedback effects from the first stars and AGN.

8. CONCLUSION

In this paper we have presented the results of the mid-infrared spectral mapping of the Stephan's Quintet system using the *Spitzer Space Telescope*. We highlight here our five main conclusions:

- The powerful H₂ emission detected by Appleton et al. (2006) surprisingly represents only a small fraction of the group-wide warm H₂ (with a lower limit luminosity of $1.1 \times 10^{42}\,\mathrm{erg\,s^{-1}}$ spread over ~ 975 kpc²) that dominates the mid-infrared emission of the system. There is evidence for another shock-excited feature, the so-called H₂ bridge between the main shock and NGC 7319, which is likely a remnant of past tidal interactions within the group. The spatial variation in the distribution of the H₂ 0-0 line ratios implies differences in temperature and excitation in the shocked system - this will be explored fully in Paper II.

- The global $L(H_2)/L_{X(0.001-10\mathrm{kev})}$ ratio in the main shock is $>= 3$, and $\sim$2.5 in the new "bridge" feature. The results confirm that MIR H₂ lines are a stronger coolant than X-ray emission over the shock structures, indicating a new cooling pathway seen on a large scale in SQ. This modifies the traditional view that X-rays dominate cooling at all times in the later stages of compact group evolution. Since H₂ forms on the surfaces of dust grains, we expect dust emission associated with these regions, but a low intensity radiation field produces only weak emission at 24μm.

- Following earlier interpretations of nebular line ratios in the optical, we interpret infrared ionic lines within the framework of fast ($V_s > 100$ km s^{-1}) ionizing shocks. Comparison between the [Ne II], [Ne III], [Si II] and [Fe II] line intensities implies that both silicon and iron are depleted onto dust. This result implies that dust is not destroyed in the shock.

- Star formation in SQ is dominated by SQ-A and 7318b-south, located at the extreme ends of the shock ridge seen at radio wavelengths, suggesting they are both shock triggered starbursts. However, regions dominated by warm H$_2$ emission exhibit very low star formation rates, consistent with a turbulent model where H$_2$ is significantly reheated and cool clouds are too short-lived or undersized to collapse.

- In SQ we observe the projected coexistence of [Si II] and H$_2$ being produced by ~ 200 km s^{-1} and ~ 20 km s^{-1} velocity shocks, respectively. Our observational results are consistent with a model of a multiphase postshock medium produced by a galaxy-wide collision (Guillard et al. 2009).

The cooling pathway of warm H$_2$ emission we observe group-wide in SQ is clearly a significant, albeit surprising, mechanism in shock systems. To determine the overall dominant cooling mechanism in SQ, we require an inventory of lines and continuum processes at all wavelengths. Early shock models (Draine et al. 1983) predict that, apart from the rotational emission from H$_2$, contributions from lines such as [O I]63.2μm, [C II]157.7μm and the THz spectrum of H$_2$0 (Pearson et al. 1991) could be significant. We hope to explore this chemistry more fully, and the detailed distribution of cool dust, using the capabilities of the *Herschel* Space Observatory. In addition, we cannot rule out strong UV line-cooling.

Stephan's Quintet provides the ideal laboratory for probing a mechanism potentially crucial in systems ranging from ULIRGs to radio galaxies to supernova remnants.

REFERENCES

Allen, M.G., Groves, B.A., Dopita, M.A., Sutherland, R.S., & Kewley, L.J. 2008, ApJ, 178, 20

Allen, R.J., & Hartsuiker, J.W. 1972, Nature, 239, 324

Allen, R.J., & Sullivan, W.T.,III. 1980, A&A, 84, 181

Appleton, P., et al. 2009, Astro2010: The Astronomy and Astrophysics Decadal Survey, Science White Papers, 2010, 2

Appleton, P.N. et al. 2006, ApJ, 639, L51

Appleton, P.N., Charmandaris, V., Horrelou, C., Mirabel, I.F., Ghigo, F., Higdon, J.L., & Lord, S. 1999, ApJ, 527, 143

Bernard-Salas, J. et al. 2009, ApJ, in press (arXiv:astro-ph/0908.2821)

Black, J. H., & van Dishoeck, E. F. 1987, ApJ, 322, 412

Bournaud, F., & Elmegreen, B. G. 2009, ApJ, 694, L158

Brandl, B.R. et al. 2006, ApJ, 653, 1129

Bromm, V., Ferrara, A., Coppi, P. S., & Larson, R. B. 2001, MNRAS, 328, 969

Buchanan, C. L., Gallimore, J. F., O'Dea, C. P., Baum, S. A., Axon, D. J., Robinson, A., Elitzur, M., & Elvis, M. 2006, AJ, 132, 401

Calzetti, D., et al., 2007, ApJ, 666, 870

Conselice, C. J., et al. 2005, ApJ, 633, 29

Dale, D.A., et al. 2006, ApJ, 646, 161

Dekel, A., Sari, R., & Ceverino, D. 2009, ApJ, 703, 785

Deo, R.P., et al. 2007, ApJ,, 671, 124

Dopita, M. A., & Sutherland, R. S. 1995, ApJ, 455, 468

Draine, B.T., Roberge, W.G., & Dalgarno, A. 1983, ApJ, 264, 485

Draine, B. T., & Woods, D. T. 1992, ApJ, 387, 732

Draine, B.T., & Li A. 2001, ApJ, 551, 807

Durret, F. 1994, A&AS, 105, 57

Egami, E., Rieke, G.H., Fadda, D. & Hines, D.C. 2006, ApJ, 652, L21

Elmegreen, B. G., & Elmegreen, D. M. 2005, ApJ, 627, 632

Förster Schreiber, N. M., et al. 2006, ApJ, 645, 1062

Gao, Y. & Xu, C. 2000, ApJ, 542, L83

Genzel, R., et al. 2008, ApJ, 687, 59

Greif, T. H., Johnson, J. L., Klessen, R. S., & Bromm, V. 2008, MNRAS, 387, 1021

Guillard, P., Boulanger, F., Cluver, M., Appleton, P.N., Pineau des Forêts, G., & Ogle, P. 2010, A&A, submitted

Guillard, P., Boulanger, F., Pineau des Forêts, G., & Appleton, P.N. 2009, A&A, 502, 515

Hatch, N.A., Crawford, C.S, Fabian, A.C., & Johnstone, R.M. 2005, MNRAS, 358, 765

Helou, G., & Bicay, M.D. 1993, ApJ, 415, 93

Hewitt, J.W., Rho, J., Andersen, M., & Reach, W.T. 2009, ApJ, 694, 1266

Ho, L.C., & Keto, E. 2007, ApJ, 658, 314

Hollenbach, D., & McKee C.F. 1989, ApJ, 342, 306

Hollenbach, D. J., & Tielens, A. G. G. M. 1997, ARA&A, 35, 179

Houck, J.R., Weedman, D.W., Le Floc'h, & Hao, L. 2007, ApJ, 671, 323

Houck, J.R. et al. 2004, ApJS, 154, 18

Kennicutt Jr., R.C., 1998, ARA&A, 36, 189

Lepp, S., & McCray, R. 1983, ApJ, 269, 560

Maloney, P.R., Hollenbach, D.J., & Tielens, A.G.G.M. 1996, ApJ, 466, 561

Martín-Hernández, N.L., Vermeij, R., Tielens, A.G.G.M., van der Hulst, J.M., & Peeters, E. 2002, A&A, 389, 286

Moles, M., Sulentic, J.W., & Márquez, I. 1997, ApJ, 485, L69

Neufeld, D. A., Hollenbach, D. J., Kaufman, M. J., Snell, R. L., Melnick, G. J., Bergin, E. A., & Sonnentrucker, P. 2007, ApJ, 664, 890

Pietsch W., Trinchieri, G., Arp, H., & Sulentic, J.W. 1997, A&A, 322, 89

Pearson J. C., De Lucia F. C., Anderson, T., Herbst, E., & Helminger P. 1991, ApJ, 379, L41

Ogle, P., Antonucci, R., Appleton, P., & Whysong, D. 2007, ApJ, 668, 699

Ogle, P. et al. 2009, ApJ, submitted

O'Sullivan, E.O., Giacintucci, S., Vrtilek, J.M., Raychaudhury, S., & David, L.P. 2009, ApJ, 701, 1560

Rieke, G. et al., 2004, ApJS, 154, 204

Rigopoulou, D., Kunze, D., Lutz, D., Genzel, R., & Moorwood, A.F.M. 2002, A&A, 389, 374

Santoro, F., & Shull, J. M. 2006, ApJ, 643, 26

Shull, J. M., & Hollenbach, D. J. 1978, ApJ, 220, 525

Simpson, J. P., Witteborn, F. C., Price, S. D., & Cohen, M. 1998, ApJ, 508, 268

Smith, J.D.T. et al. 2007, PASP, 119, 1133

Smith, J.D.T. et al. 2009, ApJ, 693, 713

Sulentic, J.W., Rosado, M., Dultzin-Hacyan, D., Verdes-Montenegro, L., Trincheri, G., Xu, C., & Pietsch, W. 2001, AJ, 122, 2993

Trinchieri, G., Sulentic, J., Breitschwerdt, D., & Pietsch, W., 2003, A&A, 401, 173

Trinchieri, G., Sulentic, J., Pietsch, W., & Breitschwerdt, D. 2005, A&A, 444, 697

Verma, A., Lutz, D., Sturm, E., Sternberg, A., Genzel, R., &
    Vacca, W. 2003, A&A, 403, 829
Weedman, D., et al. 2005, ApJ, 633, 706
Werner, M. W., et al. 2004, ApJS, 154, 1
Williams, B.A., Yun, M.S., & Verdes-Montenegro, L. 2002, AJ,
    123, 2417
Xanthopoulos, E., Muxlow, T.W.B., Thomasson, P., &
    Garrington, S.T., 2004, MNRAS, 353, 1117

Xu, C., Sulentic, J.W., & Tuffs, R. 1999, ApJ, 512, 178
Xu, C.K., Lu, N., Condon, J.J., Dopita, M., & Tuffs, R.J. 2003,
    AJ, 595, 665
Xu, C.K., et al. 2005, ApJ, 619, L95
Yun, M.S., Verdes-Montenegro, L., del Olmo, A., & Perea, J.
    1997, ApJ, 475, L21

In this Section we discuss the results pertaining to NGC 7319, a Seyfert 2 galaxy (Durret 1994) lying to the East in the SQ group (see Fig. 1). The specific intensity contours for the H_2 S(0) and H_2 S(1) lines (Fig. 2a and b) show emission associated with the galaxy, seemingly connected to the rest of the group by the H_2 "bridge" discussed in Section 3.1. Figure 3 shows that the nucleus of NGC 7319 produces strong X-ray emission (Trinchieri et al. 2003) and is prominent at radio wavelengths (Xu et al. 2003). However, we observe an offset between the peak of the H_2 emission near NGC 7319 and the Seyfert nucleus, which suggests that the "bridge" is a separate structure and not being excited by the AGN.

The AGN in NGC 7319 does not have a well-collimated jet, but two extended lobes with compact hotspots, asymmetrically distributed along the minor axis of the galaxy (Xanthopoulos et al. 2004). This structure runs NE/SW and its orientation compared to the H_2 filament (which runs EW) is not consistent with causing the excitation of the H_2 bridge. This is also evident from the relatively weak power in the AGN, as inferred by the emission line diagnostics discussed below, and in the X-ray where it is only a factor of ~ 2 greater than the emission associated with the main shock and "bridge".

In Figure 4 we present the specific intensity contours of the [Fe II]25.99μm (blended with [O IV]25.89μm), [S III]33.48μm and [Si II]34.82μm emission lines. Given the low spectral resolution of the SL and LL modules of *Spitzer*, we cannot distinguish between emission from [Fe II] and [O IV]. The AGN in NGC 7319 is likely to produce both, with [Fe II] emission likely originating in X-ray dissociation regions (XDRs) surrounding the AGN (Maloney et al. 1996). Prominent emission from [S III]33.48μm and [Si II]34.82μm are due to the high excitation conditions associated with the AGN. Dense PDRs and X-ray dominated regions, powered by AGN, show strong [Si II] emission at 34.82μm, while [S III] 33.48 μm emission acts as a tracer of H II regions.
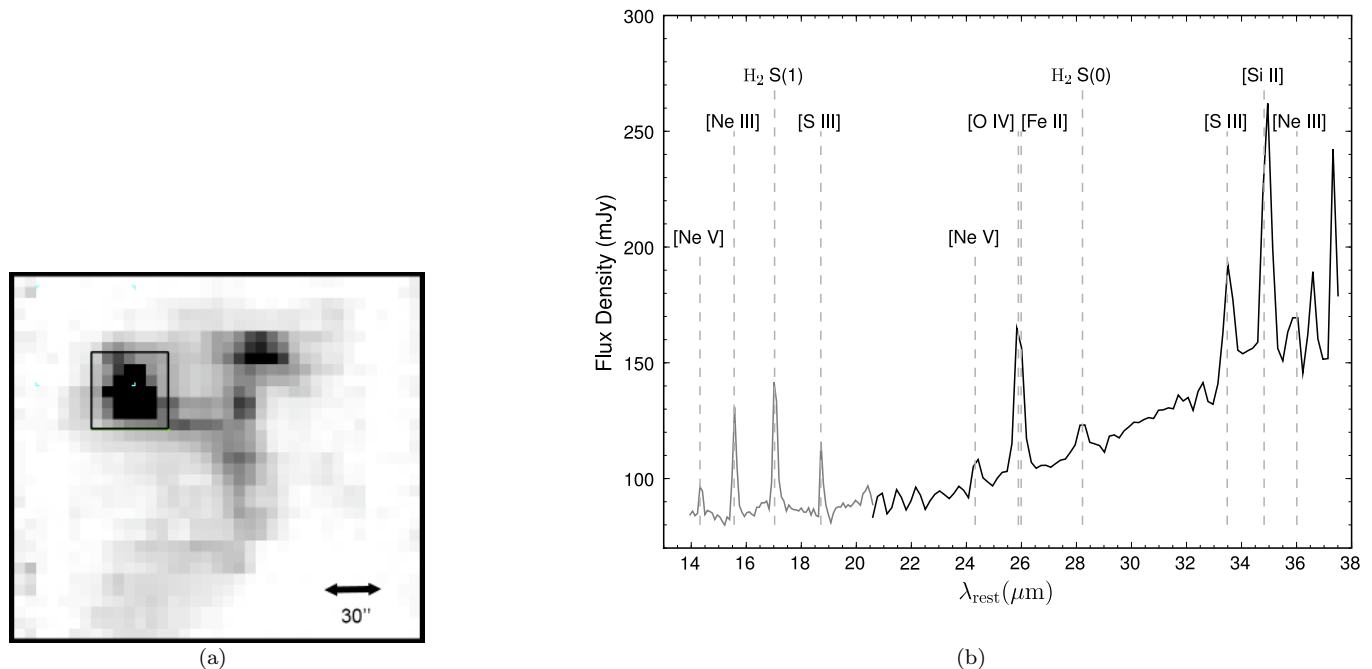

FIG. 14.— Rectangular extraction box for the Seyfert 2 galaxy NGC 7319 overlaid on the H_2 0-0 S(1) line emission (a) and the corresponding low-resolution spectrum (b). The extraction box is centered on $22^h36^m03.62^s$, $+33°58'35.6''$.

We now focus on the emission line properties of NGC 7319. Figure 14 shows the spectrum extracted from the galaxy and the measured properties of the line ratios are listed in Table 2 and 3. For the first time in the SQ group, we observe a spectrum which is no longer dominated by H_2 emission, but instead the brightest lines are the high-excitation [O IV]25.91μm and [Fe II]25.98μm blended lines, as well as the [Si II]34.81μm line. [Ne V] is prominent at both 14.32μm and 24.30μm – a line typically seen in AGN. Also, unlike the majority of the extended shocked regions, there is a rising thermal continuum more typical of a starforming galaxy than a classical Seyfert galaxy, although as various studies have shown (Buchanan et al. 2006 ; Deo et al. 2007), Seyfert II galaxies exhibit a variety of MIR spectral characteristics at long wavelengths. NGC 7319's rising continuum is similar to that seen in the Seyfert II galaxy NGC 3079 (Deo et al. 2007), and likely represents a dominant starburst component in the Far-IR. Spitzer imaging reveals not only a bright nucleus, but also extended emission regions in the galaxy.

Using the [Si II]34.81μm/[S III]33.48μm ratio as a probe of excitation sources, we find a ratio of ~ 1.85 which is low compared to the average value found for AGN galaxies (~ 2.9) in the *Spitzer* Infrared Nearby Galaxy Sample (SINGS),

but high compared to star-forming regions (~ 1.2) in the same sample (Dale et al. 2006). This suggests a relatively weak AGN. The [Ne III] 15.56μm/[Ne II] 12.81μm ratio is a measure of radiation field strength and the value of 0.97 indicates a typical radiation field strength compared to other AGN (the sample of Weedman et al. 2005 shows a range of ~ 0.17 to 1.9). The average electron density, estimated from the [S III]18.71μm/[S III]33.48μm ratio of ~ 0.56, is $100 - 200$ cm^{-3} (Martín-Hernández et al. 2002), in the low-density limit for this diagnostic (Smith et al. 2009).

The properties of the H₂ emission of NGC 7319 are limited to the two long wavelength lines observed by IRS-LL (the galaxy lies outside the region mapped by SL). As a result, the excitation diagram contains only two points allowing only an approximate idea of the H₂ mass, since without the SL wavelength coverage to provide information on possible warmer components, we are likely to overestimate the temperature of the H₂ by fitting a straight line to the points. Any warmer component would contribute to the flux of the 0-0 S(1) line thus leading to a reduction of the temperature (and increase in H₂ mass) for any cooler component. However, to provide a guide, we estimate the temperature of H₂ $<=171\pm8$ K (assuming the gas is in thermal equilibrium and thus an ortho-para ratio of 2.65) and a total H₂ mass of $3.0\pm7\times10^{8}$ M$_{\odot}$. We consider this a lower limit to the total warm mass if (as is likely) more than one component is present. Gao & Xu (2000) estimated the *cold* molecular hydrogen mass of NGC 7319 based on ^{12}CO (1-0) observations as $> 3.6 \times10^{9}$ M$_{\odot}$, a factor of roughly ten greater than the warm H₂ mass. Such a ratio is not atypical of large spiral galaxies Rigopoulou et al. (2002).

APPENDIX B: HIGH RESOLUTION SPECTRUM OF SHOCK CENTRE REANALYSED

The high resolution spectrum at the center of the shock in SQ, obtained by Appleton et al. (2006), has been reanalysed using the latest calibrations available for the IRS instrument (SSC pipeline version S17) and is included as Figure 15. This has shown that the H₂ gas lies at a velocity of $6360(\pm100)$ km s^{-1}, between the velocity of the group (6600 km s^{-1}) and the velocity of the intruder (5700 km s^{-1}). This is consistent with a model of gas being accelerated by the shock, as well as the turbulence demonstrated by the broad linewidth of the H₂ in the shock (860 km s^{-1}).
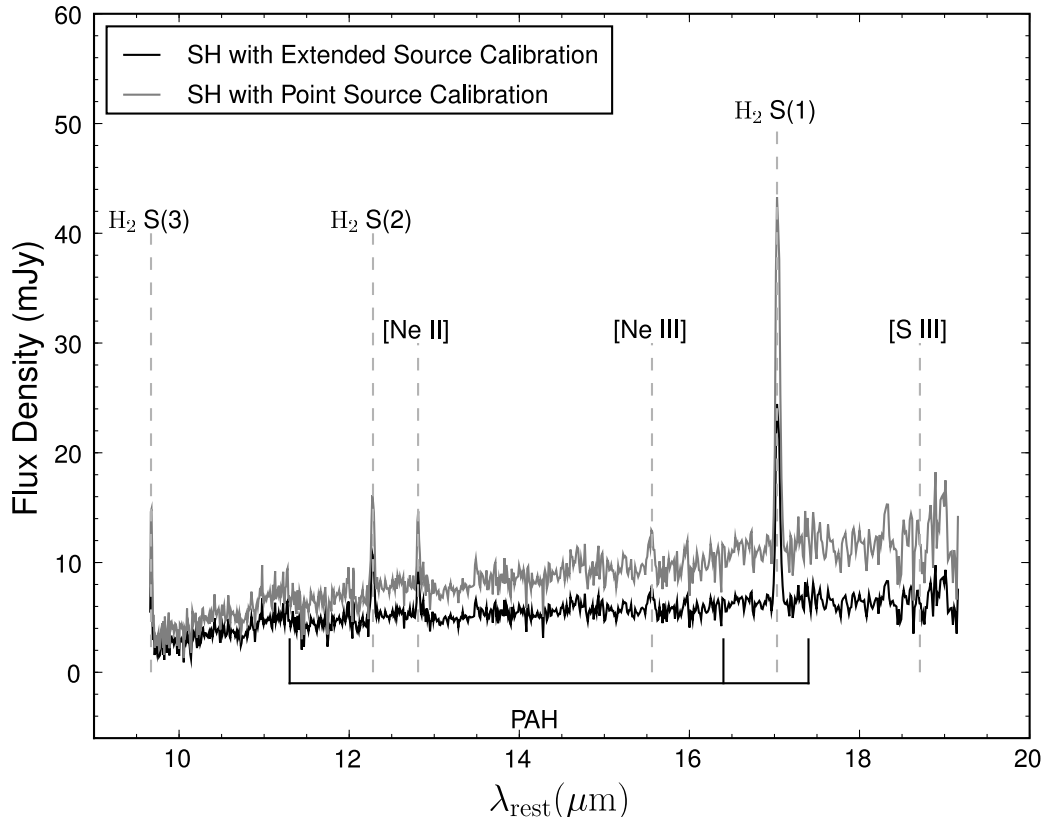
FIG. 15.— *Spitzer* Short-High (SH) Spectrum, centred on $22^{\rm h}35^{\rm m}59.57^{\rm s}$, $+33^{\circ}58'1.8''$, reanalysed using the latest point source and extended source calibrations.

The new SH spectrum shows that with the improved calibrations, the 11.3μm PAH feature is detected, although faint. This is consistent with what is found in the larger extractions that show enhanced 11.3μm PAH emission compared to ionised PAH features emitting at 6.2μm and 7.7μm.

APPENDIX C: X-RAY FLUXES IN EXTRACTED REGIONS

In this section we present the X-ray fluxes in the extraction regions shown in Figure 7. The reanalysis of archival data is necessary to obtain accurate fluxes and luminosities for the X-ray emission over the various apertures matched to our spectral extractions. We use the XMM-Newton EPIC-pn data (see Trinchieri et al. 2005, for observational details) to obtain the most sensitive measurements. A calibrated event file was generated and filtered using standard quality flags, and subsequently cleaned of background flares. A 0.3–2 keV image was then extracted and corrected for instrumental response. All point-like sources were masked out to $25''$ in the analysis of diffuse emission, and the local background level was estimated within a 5×9 arcmin^2 rectangular region away from the group core. For each region in Fig. 7, resulting background-subtracted photon count rates were converted to 0.3–2 keV and "bolometric" (0.001–10 keV) X-ray fluxes assuming an absorbed thermal plasma model of metallicity 0.4 Solar, with temperature as estimated from the map of O'Sullivan et al. (2009), and an absorbing Galactic H I column density of $N_{\rm H} = 6.2 \times 10^{20}$ cm^{-2}. For NGC 7319, which harbors an AGN, an absorbed power-law spectrum of photon index $\Gamma = 1.7$ was assumed instead. Results are listed in Table 1.

TABLE 1
X-ray Count Rates and Fluxes for Extracted Regions

Region	Count Rate (0.3-2 keV) (photons s^{-1})	Flux (0.3-2 keV) erg s^{-1} cm^{-2}	Bolometric Flux (0.001-10 keV) erg s^{-1} cm^{-2}	Adopted Spectral Model
Main Shock	0.102	1.8×10^{-13}	2.8×10^{-13}	$T = 0.7$ keV
Shock Sub-region	0.017	3.3×10^{-14}	5.1×10^{-14}	$T = 0.8$ keV
Bridge	0.017	3.0×10^{-14}	4.5×10^{-14}	$T = 0.6$ keV
NGC 7319	0.051	1.1×10^{-13}	3.7×10^{-13}	$\Gamma = 1.7$
SQ-A	0.013	2.4×10^{-14}	3.7×10^{-14}	$T = 0.6$ keV

Note. — Statistical uncertainties on all flux measurements are $< 10\%$.

We note that for the main shock (with luminosity 1.9×10^{41} erg s^{-1} in the 0-3-2 keV band) we are within a factor of 2 of the 0.5-2 keV luminosity $\sim 3.1 \times 10^{41}$ erg s^{-1} obtained for a similar, but larger extraction of the shock by Trinchieri et al. (2005). O'Sullivan et al. (2009) obtain a 0.5-2 keV surface brightness of 0.07 L$_\odot$ pc^{-2} in the main shock compared to our value of 0.1 L$_\odot$ pc^{-2} for the 0.3-2 keV surface brightness.

TABLE 2
Observed H₂ Line Fluxes in units of 10^{-17} W m^{-2}

Target Region	Aperture (arcsec²)	H₂ 0-0 S(0) $\lambda28.22\mu$m	H₂ 0-0 S(1) $\lambda17.03\mu$m	H₂ 0-0 S(2) $\lambda12.28\mu$m	H₂ 0-0 S(3) $\lambda9.66\mu$m	H₂ 0-0 S(4) $\lambda8.03\mu$m	H₂ 0-0 S(5) $\lambda6.91\mu$m
Main Shock	2307	3.09±0.19	23.05±0.26	9.10±0.38	22.76±0.84	2.5±1.0	14.1±0.7
Shock Sub-region	242	0.36±0.03	3.13±0.02	1.47±0.08	3.60±0.08	1.04±0.15	2.37±0.30
Bridge	413	0.72±0.04	4.94±0.09	⋯	⋯	⋯	⋯
NGC 7319	1302	2.06±0.26	11.00±0.48	⋯	⋯	⋯	⋯
SQ-A	671	1.83±0.05	8.8±0.13	⋯	⋯	⋯	3.7±0.93

Note. — Upper limits are the 3σ values calculated from the RMS (root mean square) and the expected line profile width.
.

TABLE 3
Observed Fine Structure Line Fluxes in units of 10^{-17} W m^{-2}

Target Region	[Ne II] $\lambda12.81\mu$m	[Ne V] $\lambda14.32\mu$m	[Ne III] $\lambda15.56\mu$m	[S III] $\lambda18.71\mu$m	[Ne V] $\lambda24.32\mu$m	[Fe II]+[O IV] $\lambda25.99+25.89\mu$m	[S III] $\lambda33.48\mu$m	[Si II] $\lambda34.82\mu$m
Main Shock	5.31±0.30	<0.9	1.94±0.39	0.76±0.13	<0.14	1.07±0.10	1.87±0.15	8.59±0.27
Shock Sub-region	1.04±0.09	<0.18	0.15±0.06	<0.12	<0.14	0.15±0.03	0.13±0.02	1.23±0.04
Bridge	⋯	⋯	0.39±0.04	<0.1	<0.15	0.29±0.04	<0.22	1.1±0.1
NGC 7319	⋯	2.89±0.64	9.47±0.29	2.81±0.40	1.56±0.39	10.9±0.27	5.0±0.42	9.24 ±0.49
SQ-A	⋯	<0.8	1.29±0.16	0.87±0.06	<0.18	<0.17	1.54±0.10	2.3±0.16

Note. — Upper limits are the 3σ values calculated from the RMS and the expected line profile width.
.